Tran-SET

Transportation Consortium of South-Central States

Solving Emerging Transportation Resiliency, Sustainability, and Economic Challenges through the Use of Innovative Materials and Construction Methods: From Research to Implementation

Coupling Novel Soil Moisture-Suction Sensors and UAV Photogrammetry Technology to the Performance of Highway Embankments

Project No. 19GTLSU05

Lead University: Louisiana State University

Collaborative Universities: University of Texas at Arlington and Texas A&M University

Final Report

October

2021

Disclaimer

The contents of this report reflect the views of the authors, who are responsible for the facts and the accuracy of the information presented herein. This document is disseminated in the interest of information exchange. The report is funded, partially or entirely, by a grant from the U.S. Department of Transportation's University Transportation Centers Program. However, the U.S. Government assumes no liability for the contents or use thereof.

Acknowledgements

The authors would like to thank the Transportation Consortium of South-Central States (Tran-SET) for the funding necessary for this research. The authors would also like to thank the Louisiana Department of Transportation and Development (LADOTD) for their assistance.

TECHNICAL DOCUMENTATION PAGE

1. Project No.	2. Government Accession No.	3. Recipient's Catalog No.
19GTLSU05		

4. Title and Subtitle	5. Report Date
Coupling Novel Soil Moisture-Suction Sensors and UAV Photogrammetry Technology to the Performance of Highway Embankments	Oct. 2021
	6. Performing Organization Code
7. Author(s)	**8. Performing Organization Report No.**
PI: Navid H. Jafari https://orcid.org/0000-0002-4394-3776 Co-PI: Anand J. Puppala https://orcid.org/0000-0003-0435-6285 Co-PI: Xinbao Yu https://orcid.org/0000-0002-5681-0390 Co-PI: Surya Sarat Chandra Congress https://orcid.org/0000-0001-5921-9582	
9. Performing Organization Name and Address	**10. Work Unit No. (TRAIS)**
Transportation Consortium of South-Central States (Tran-SET) University Transportation Center for Region 6 3319 Patrick F. Taylor Hall, Louisiana State University, Baton Rouge, LA 70803	**11. Contract or Grant No.** 69A3551747106
12. Sponsoring Agency Name and Address	**13. Type of Report and Period Covered**
United States of America Department of Transportation Research and Innovative Technology Administration	Final Research Report Aug. 2019 – Feb. 2021
	14. Sponsoring Agency Code

15. Supplementary Notes

Report uploaded and accessible at Tran-SET's website (http://transet.lsu.edu/).

16. Abstract

The movement of water plays a critical role in the mechanical performance and service life of transportation infrastructure, especially for pavement subgrades and highway embankments consisting of high-plasticity, expansive soils that saturate and ultimately lead to infrastructure distress. Shallow slides along highway embankments are ubiquitous across Region 6 because long-term wetting and drying cycles considerably weaken these compacted soils. In the aftermath of heavy rains, pore-water pressures increase to a critical threshold such that a failure occurs. The implications of embankment failures range from repeated maintenance repairs to long-term road closures. A comprehensive approach to model highway embankments comprising of laboratory testing, setup, and field data collection using unmanned aerial vehicles has been proposed in this study.

17. Key Words	18. Distribution Statement
Slope stability, embankments, unmanned aerial vehicles	No restrictions. This document is available through the National Technical Information Service, Springfield, VA 22161.

19. Security Classif. (of this report)	20. Security Classif. (of this page)	21. No. of Pages	22. Price
Unclassified	Unclassified	38	

Form DOT F 1700.7 (8-72) **Reproduction of completed page authorized.**

SI* (MODERN METRIC) CONVERSION FACTORS

APPROXIMATE CONVERSIONS TO SI UNITS

Symbol	When You Know	Multiply By	To Find	Symbol
		LENGTH		
in	inches	25.4	millimeters	mm
ft	feet	0.305	meters	m
yd	yards	0.914	meters	m
mi	miles	1.61	kilometers	km
		AREA		
in^2	square inches	645.2	square millimeters	mm^2
ft^2	square feet	0.093	square meters	m^2
yd^2	square yard	0.836	square meters	m^2
ac	acres	0.405	hectares	ha
mi^2	square miles	2.59	square kilometers	km^2
		VOLUME		
fl oz	fluid ounces	29.57	milliliters	mL
gal	gallons	3.785	liters	L
ft^3	cubic feet	0.028	cubic meters	m^3
yd^3	cubic yards	0.765	cubic meters	m^3
		NOTE: volumes greater than 1000 L shall be shown in m^3		
		MASS		
oz	ounces	28.35	grams	g
lb	pounds	0.454	kilograms	kg
T	short tons (2000 lb)	0.907	megagrams (or "metric ton")	Mg (or "t")
		TEMPERATURE (exact degrees)		
^oF	Fahrenheit	5 (F-32)/9 or (F-32)/1.8	Celsius	^oC
		ILLUMINATION		
fc	foot-candles	10.76	lux	lx
fl	foot-Lamberts	3.426	candela/m^2	cd/m^2
		FORCE and PRESSURE or STRESS		
lbf	poundforce	4.45	newtons	N
lbf/in^2	poundforce per square inch	6.89	kilopascals	kPa

APPROXIMATE CONVERSIONS FROM SI UNITS

Symbol	When You Know	Multiply By	To Find	Symbol
		LENGTH		
mm	millimeters	0.039	inches	in
m	meters	3.28	feet	ft
m	meters	1.09	yards	yd
km	kilometers	0.621	miles	mi
		AREA		
mm^2	square millimeters	0.0016	square inches	in^2
m^2	square meters	10.764	square feet	ft^2
m^2	square meters	1.195	square yards	yd^2
ha	hectares	2.47	acres	ac
km^2	square kilometers	0.386	square miles	mi^2
		VOLUME		
mL	milliliters	0.034	fluid ounces	fl oz
L	liters	0.264	gallons	gal
m^3	cubic meters	35.314	cubic feet	ft^3
m^3	cubic meters	1.307	cubic yards	yd^3
		MASS		
g	grams	0.035	ounces	oz
kg	kilograms	2.202	pounds	lb
Mg (or "t")	megagrams (or "metric ton")	1.103	short tons (2000 lb)	T
		TEMPERATURE (exact degrees)		
^oC	Celsius	1.8C+32	Fahrenheit	^oF
		ILLUMINATION		
lx	lux	0.0929	foot-candles	fc
cd/m^2	candela/m^2	0.2919	foot-Lamberts	fl
		FORCE and PRESSURE or STRESS		
N	newtons	0.225	poundforce	lbf
kPa	kilopascals	0.145	poundforce per square inch	lbf/in^2

TABLE OF CONTENTS

LIST OF FIGURES

ACRONYMS, ABBREVIATIONS, AND SYMBOLS

DOT	Department of Transportation
FEM	Finite Element Method
FOS	Factor of Safety
LEM	Limit Equilibrium Method
LSU	Louisiana State University
UTA	University of Texas at Arlington

EXECUTIVE SUMMARY

The movement of water plays a critical role in the mechanical performance and service life of transportation infrastructure, especially for pavement subgrades and highway embankments consisting of high-plasticity soils that saturate and ultimately lead to infrastructure distress. In the aftermath of heavy rains, pore-water pressures increase to a critical threshold such that a failure occurs. The implications of embankment failures range from repeated maintenance repairs to long-term road closures. The proposed research will advance the understanding of how long-term wetting-drying cycles change the in-situ unsaturated and strength properties of high-plasticity clays and how heavy rains infiltrate into embankments and increase pore-water pressures that ultimately cause shallow slides. Furthermore, it is unknown why shallow slides occur in localized areas of an embankment and how to incorporate unmanned aerial vehicles (UAVs) in visualizing and documenting geotechnical assets. The proposed research also leverages novel sensors to address in-situ moisture and suction measurement in embankments. The findings of this study are aimed to promote more resilient geotechnical infrastructure and use emerging technologies to possibly extend the service life and repair earth embankments. In particular, novel sensors that combine soil moisture and suction will be used to evaluate in-situ unsaturated and saturated conditions of highway embankments. Moreover, UAV technology will be leveraged with photogrammetry for data collection to predict highway embankment performance under climate extremes.

The overarching objective of this research is to develop a comprehensive approach to model highway embankments comprising of laboratory testing, setup, and field data collection using unmanned aerial vehicles. The proposed project scope focuses on developing a predictive design and rehabilitation tool for highway embankments while addressing fundamental unsaturated and shear strength research questions. The selected site is located near the Highway I-10 – Blue Bonnet intersection in Baton Rouge, Louisiana. The coordinates of the embankment are 30°23'40.4"N, 91°05'08.2"W. Native soils at this site were classified as high plasticity clay. The embankment is located on the right side of eastbound Highway I-10 and is approximately 20 ft high.

The objective of this research project is to:

1. Measure in-situ suction and moisture content using a novel suction-TDR sensor,
2. Rapidly evaluate embankment geometry and slope movements using unmanned aerial vehicles (UAVs), and
3. Implementation of research results along with workforce development and education.

1. INTRODUCTION

1.1. Slope Stability

Skempton (*1*) studied and reported about the high plasticity London clays. He also introduced the concept of fully-softened shear strength and explained how wetting-drying cycles can reduce the shear strength of the clay to its fully-softened value. This is a common type of slope failure after heavy and prolonged rainfall events. Wright (*2*) explained that these shallow failures in expansive clays often occur within the top 1 to 2 m of the slope and the failure surface is parallel to the slope face.

Puppala et al. (*3*) presented the results of diverse tests performed on low and high plasticity clays in Texas. The samples were obtained from El Paso, Fort Worth, Paris, San Antonio, and Houston, Texas. They conducted basic soil property tests, chemical tests, and engineering tests. The results showed that the soils exhibiting high plasticity index properties contained moderate to large amounts of montmorillonite, whereas the soil exhibiting low plasticity index properties contained small amounts of montmorillonite. As expected, only the high plasticity clays experienced large volume changes when swelling and shrinkage tests were performed. All these results emphasize the importance of knowing the characteristics of high plasticity, expansive clay, and how it can affect road embankments and other structures when exposed to wetting-drying cycles.

George et al. (*4*) presented the results of a shallow slope failure in North Texas. As in many road embankments built with expansive clays, shallow slope failures in these structures are likely seen due to wetting-drying cycles and subsequent formation of desiccation cracks after alternate cycles of rainfall events followed by droughts. The slope stability analysis was performed on three scenarios: (1) short-term post-construction condition of the slope, (2) condition with the maximum water table in the slope, and (3) condition with the maximum water table in the slope and desiccation cracks formed at the surface layer. In the third scenario, the desiccation cracks were included in the analysis along with the maximum water table level, which exhibited the lowest FS equal to 0.85. The overall analysis indicated how expansive clays in road embankments change their behavior when subjected to wetting-drying cycles.

1.2. Infrastructure Monitoring

The durability of infrastructure is influenced by different factors, such as the loading and environmental conditions, rate of utilization, and frequency of unforeseen events. Maintenance of infrastructure, in a timely and proactive manner, will not only enhance the durability of the infrastructure asset but also gives a higher return on investment. Conventional data collection methods used for assessing the infrastructure condition are subjective, laborious, and may cause frequent interactions between working personnel and live traffic. Thus, there is a need to identify a technology that will provide quick, repeatable, and reliable data safely.

1.2.1. Aerial Data Collection

Photogrammetry is the science of making measurements using two or more images collected remotely. Various terrestrial and aerial platforms are used to mount the sensors capable of obtaining high-quality images with multiple views of an object under inspection. These platforms vary from a smartphone camera to sensors mounted on a satellite. Close Range Photogrammetry (CRP) deals with measuring distances from the imagery of the object captured within a distance

of 1000 ft from the sensors (*5, 6*). In the recent past, advancements in unmanned aerial platforms paralleled with the development of portable and high-quality sensors have promoted the application of unmanned aerial vehicle (UAV) technology for infrastructure condition assessment and management.

Many previous studies have reported the ubiquitous application of UAVs in various domains such as surveillance and control of maritime traffic, construction monitoring, terrain mapping, fire disasters, infrastructure monitoring, slope stability, detection and control of coastal hazards, flood monitoring, earthquake damage assessment, and post distress monitoring survey (*7-16*). Unmanned Aerial Vehicle-Close Range Photogrammetry (UAV-CRP) technology was used to collect the surficial geometry of the embankment and perform slope stability analysis in conjunction with the laboratory testing results.

2. OBJECTIVES

The overarching objective of this research is to develop a comprehensive approach to model highway embankments comprising of laboratory testing, setup, and field data collection using unmanned aerial vehicles.

The proposed project scope focuses on developing a predictive design and rehabilitation tool for highway embankments while addressing fundamental unsaturated and shear strength research questions.

The objective of this research project is to:

1. Measure in-situ suction and moisture content using a novel suction-TDR sensor,
2. Rapidly evaluate embankment geometry and slope movements using unmanned aerial vehicles (UAVs), and
3. Implementation of research results along with workforce development and education.

3. LITERATURE REVIEW

3.1. In-situ Soil Moisture Sensors

In-situ soil moisture measurement has advanced significantly in the last decade. Among those many available techniques, Time Domain Reflectometry (TDR) moisture sensors have proven to be the most reliable and widely used one for point measurement of in-situ moisture sensors (*17*). TDR sensors utilize guided electromagnetic waves to measure the dielectric constant and electrical conductivity of soils that are directly related to soil moisture and density. It works by measuring the material response to small-magnitude electromagnetic field excitation. Based on the TDR technique, Drnevich et al. (*18*) developed a "one step method" to estimate the soil moisture content and dry density simultaneously from the soil dielectric constant (K_a) and electrical conductivity (EC_b), which are analyzed and obtained from the reflected TDR waveforms (*19*). In geotechnical engineering, it is necessary to properly monitor in-situ soil compaction properties during most of earthwork construction projects. The conventional in-situ soil compaction monitoring methods are always limited in their applications, whereas the TDR technique is the one that can better achieve the above goal in the field (*20*). It can be used to measure both in-situ moisture content as well as dry density by the propagation of an electromagnetic wave going through the soils, and it has been implemented in many fields with success for applications in geotechnical engineering.

3.1.1. Soil Suction Sensors

Soil water characteristic curve (SWCC) defines the relationship between water content (θ or w) and soil matric suction (ψ), which is important to characterize the soil behavior under unsaturated conditions. Soil matric suction is usually measured either by direct or indirect measurement techniques. Direct suction measurement methods include the tensiometer method, tempe pressure cell method, pressure plate extractor method, and filter paper method. Indirect suction measurement techniques mainly include TDR, thermal conductivity sensor (TCS), and electrical conductivity sensor (*21*). For water potential in the specific range, the heat dissipation method, filter paper method, or gypsum block electrical-resistance method may be used in the laboratory and in the field (*22*). Nevertheless, determining SWCC in the field still remains a challenge due to the limitations of the existing methods. For example, soil matric suction is often measured by a tensiometer limited to a measuring range from 0 to 85 kPa (*23*). Additionally, thermocouple psychometry can be used to measure soil matric suction in a wide range but it is very sensitive to temperature change (*22*).

Noborio et al. (*24*) indicated that measuring water content, thermal/electrical properties of a constructed porous medium equilibrated with surrounding soils is another attempt to indirectly measure soil matric suction. The porous medium needs to be first calibrated to establish a relationship between the measured properties and its matric suction, then the soil suction can be measured indirectly. On the other hand, the TDR technique has been successfully demonstrated to be a reliable method to measure soil moisture content both in the laboratory and in the field (*19, 25-28*). In the studies of Baumgartner et al. (*29*) and Whalley et al. (*30*), porous materials, functioning as tensiometers, were attached to the end of hollow electrodes of the TDR probe for simultaneous measurements of soil moisture content and matric suction. However, the same limitation as the tensiometer exists, which is the need to supply water to the tensiometer, and the limited measuring range of 0 to 85 kPa. In addition, it is also reported that the TDR technique had been applied to a commercial product for estimating soil matric suction by measuring dielectric

constant (K_a) of an equilibrated porous medium (e.g., Equitensiometer, Delta-T Devices, Cambridge, England). Hence, an additional probe for moisture content measurement can be added for simultaneous measurements of soil moisture content and matric suction in a wider range.

The use of porous material sensors for matric potential measurement has been studied extensively (*24*, *31*-*34*). The soil matric suction can be measured either directly using tensiometers or indirectly using thermal conductivity and gypsum block sensors. Measurement range, accuracy, repeatability, response time, and spatial resolution of specific sensors are important considerations to their potential applications and in the analysis of soil water measurements (*35*). Gypsum block based sensors have a typical measurement range from -30 kPa to -1000 kPa. The problems of these sensors are limited temporal stability, a long response time, appreciable hysteresis, and the need for individual calibration.

3.2. Slope Stability

Two-dimensional (2D) stability analysis methods are most commonly followed by practitioners due to their simplified nature. The conservative approach of using the 2D analysis worked satisfactorily for most of the cases, but three-dimensional (3D) analysis is needed whenever there is a complex geometry with complicated boundary conditions. A comprehensive slope geometry data is hence an important part of this stability analysis. There is a need for adopting a data collection technology that collects information in less time, cost, and personnel needed in the field. In this project, UAV-CRP technology was used to obtain the geometry of the failed embankment slope.

3.2.1. Limit Equilibrium Stability Analysis

Many previous studies have conducted extensive studies on the use of 2D stability analysis. In the following sections, a literature review on slope stability analysis methods is provided with an emphasis on the use of 3D stability analysis methods. Several 3D slope stability analysis methods based on limit equilibrium analysis were proposed by previous studies (*36*, *37*). Since the geometry in the third direction might vary, the current study addresses this problem by using a detailed 3D model of the embankment for 3D stability analysis.

3.2.2. 2D vs 3D Slope Stability Analysis

During the first decade of the 21st century, the development in processors complemented by the advancement in computational capabilities led to the widespread application of 3D analysis for evaluating complex slope geometries (*7*, *38*-*40*). Lorig and Varona (*41*) stated that, in a few cases, 2D model construction and simulation require more time and effort than a 3D model for the same slope. Many researchers found that 2D analysis is more conservative than 3D analysis (*42*, *43*). For normal slopes, many researchers observed that the factor of safety (FOS) obtained from the 3D analysis is greater than the 2D analysis (*42*-*45*). Gitirana et al. (*46*) conducted 2D and 3D limit equilibrium analyses on the Lodalen landslide, Oslo, and found that the FOS from the 3D analysis was 23% higher than the 2D analysis. Leong and Rahardjo (*42*) conducted 2D and 3D analyses of the Bukit Batok slope, Singapore. The 3D analysis was conducted on an extended 2D cross-section of the slope and found that the difference between FOS obtained by 2D and 3D slope stability analyses was less than 10%. Wines (*47*) considered the same input properties for 2D and 3D analyses of a slope and obtained different safety factor values. Bolla and Paronuzzi (*48*) performed both 2D and 3D conventional limit equilibrium and numerical modeling analyses on unstable rock

slopes located in Italy and observed that the FOS from the 3D analysis was higher than the 2D analysis.
Leong and Rahardjo (*42*) mentioned three reasons for not commonly using 3D slope stability analysis. Firstly, geotechnical engineers believe that 2D slope stability analysis is more conservative than 3D analysis. Secondly, 3D slope stability analysis is more complex and time-consuming than 2D analysis. Thirdly, 3D slope stability analysis needs more input data, and visualization of output is difficult. With the widespread use of 3D analysis, the first concern can also be addressed by realizing the value of cost savings by performing 3D analysis, over 2D analysis, and still ensuring safety by considering allowable risk. The availability of high-performance computing tools and aerial data collection sensors addresses the last two concerns. The below sections discuss more about the use of aerial platforms for infrastructure data collection.

3.2.3. Numerical Tools for Stability in Highway Embankments

Assessing the stability of soil structures is one of the main components of geotechnical engineering. Research and experimentation have led to the development of several methods to predict the stability of structures such as dams, embankments, levees, slopes, etc. These methods were, at first, performed manually but the implementation of computer analyses has been possible due to the growing availability of such tools (*49*). For slope stability analysis, Limit Equilibrium Method (LEM) and Finite Elements Methods (FEM) are the most used ones. Slope stability analysis becomes critical as most of the highway embankments in Louisiana and Texas are built using medium to high expansive clays and these are known to be prone to stability problems.

The application of these analyses is primarily to estimate a Factor of Safety (FOS) to determine if the slope is safe or not. Several phenomena have been evaluated throughout the years. The effect of rainfall intensity, duration, and slope angle on the FOS of slopes was studied by Egeli et al (*50*). The soil characteristics were determined via laboratory tests and physical models were built to account for varying slope angles, relative density of soils, and initial water contents. FEM models were also performed to determine the effect of these varying characteristics on FOS. The results from the numerical modeling showed similar behavior to that of the physical models.

Different materials can be integrated into the models and taken into account to determine FOS and how these additions affect the performance of the structure (*51*). Khan and Abbas (*51*) incorporated the addition of fly ash and geogrid to an embankment to evaluate how these materials affect the embankment's performance. The analysis was made using FEM that calculated FOS, vertical and horizontal settlements, and stresses in the soil mass and additionally, it allowed the user to input construction stages to consider consolidation of the proposed embankment.

A hydrological-geotechnical model interface was created to calculate surface pore water pressure along the length of a slope, and at any time interval (*52*). The purpose was to accurately predict the changes in pore water pressure within a slope in response to given weather conditions. The hydrological model was run with current weather data from the site and then coupled with a geotechnical embankment simulation with calculated pore water pressures. It was found that permeability is crucial in determining pore water pressures, horizontal displacements, and overall performance of the embankment. The FEM analysis was carried out to show how seasonal cyclic stress changes caused outward movement, strain softening, and eventual collapse, depending on the severity and number of shrink-swell cycles. It was also determined that laboratory models and even in-situ permeability testing may be limited to determine pore water pressures in FEM. Weather data is determinant for these analyses.

Another important component of numerical modeling is the ability to perform a back analysis to determine the slip surface, soil properties in embankments or slopes, and other parameters. A landslide in a highway embankment in Oklahoma was studied for this purpose (*53*). The landslide was surveyed, the extents were delineated, and the field investigation was carried out to obtain samples for laboratory testing. Once all the preliminary activities were done, the back analysis numerical modeling was performed to verify slip surface location and its soil properties. The groundwater level was also determined, and conclusions can be drawn as to why and how the landslide occurred. A similar analysis to this was performed on a shallow slope failure in North Texas by Khan et al. (*54*). The soil parameters, geometry of slope and weather conditions were obtained for the site to perform the stability analysis. At first, an acceptable FOS was obtained even considering that the clay had reached a fully-softened shear strength at the top of the slope. A more comprehensive analysis was performed considering a perched water condition at the crest of the slope, which produced a FOS near to 1, and the failure surface plane matched that of the actual slope. The analysis proved to be a great tool to better understand what has happened and predict what may happen in future slopes. Additionally, the numerical model is a great tool to assess a repair/rehabilitation methodology for the embankment.

Cerato et al. (*55*) collected data for more than 100 slopes in Oklahoma. The slopes were categorized with susceptibility values ranging from 0 to 1 (0 being not at risk of landslide and 1 being highly susceptible to landslide) for factors such as slope angle, elevation, land cover type, soil texture, amongst others. Additionally, one of these slopes was selected to be instrumented and monitored constantly. Sensitivity analyses were performed with slope stability analysis software to determine the FOS of the slope when varying one or more parameters. The slope stability analysis, although it has its limitations, was shown to provide good predictive skills. In some cases, for example, the sensitivity analysis for the slope was set up to determine the FOS if the friction angles vary certain degrees. In the same way, for another analysis, soil cohesion was varied, and all other parameters remained constant to determine the FOS. This proves to be an important tool of the available numerical tools to predict soil stability.

Numerical modeling can also aid in the decision of implementing new techniques for highway embankment stabilization. For example, the use of prefabricated structural members constructed from steel pipe, timber, plastic, and precast concrete is being studied to prevent slope failures (*56*). The results have shown that several methods can be implemented. Although they are all effective, some are most cost-effective than others. Some of the new techniques to stabilize surficial slope failures using vertical members are installing small structural members by conventional methods, launched soil nails, or earth anchoring systems. The performance of each of these options is being studied using numerical methods for slope stability of different soils and slope parameters in Wisconsin, in both dry and saturated conditions. There are still no long-term field performance data, but the analyses so far have presented increased FOS and elimination of surficial slope failures in most cases.

Other soil stabilization options in highway embankments may include soil bioengineering methods. These methods are environmentally attractive and cost-effective. Wu et al. (*57*) implemented live poles for the stabilization of a shallow slope failure in Ohio. Poplar and willow poles were used to increase the shear strength of the slope. A preliminary slope stability analysis was performed and FOS for seepage vertical and parallel to the slope were equal or less than 1.0. Including live poles would increase the shear strength by 25 kPa and the FOS would also increase to values ranging from 1.0 for parallel seepage and 1.5 for vertical seepage. Observations were

made over a 4-year period and it was determined that the FOS depends on groundwater level, depth of the failure surface, and even poles root growth. For groundwater at the surface and parallel seepage, the slope remains unstable. Nevertheless, the FOS is much greater than 1.0 with substantial root growth. The slope stability analyses were crucial to examine the interest area before and after implementation of the solution and predict how the slope will behave during the entire process.

3.3. Photogrammetry

Remote sensing is a method of collecting data without making any physical contact with the object under inspection. Modern-day remote sensing kicked off with the invention of the camera and continued on to the invention of advanced satellite-mounted sensors. Photogrammetry is the art and science of measuring distances from multiple images of the object collected in different viewpoints (*6*). Close-range photogrammetry (CRP) using aerial platforms can generate dense point cloud images, orthomosaics, digital elevation models (DEMs), and digital terrain models (DTMs) in a short time period. Various sensors such as optical, infrared, and multispectral cameras are mounted on terrestrial and aerial platforms to conduct a qualitative and quantitative inspection of the infrastructure assets (*58*).

3.3.1. Unmanned Aerial Vehicle Systems

Unmanned aerial vehicle systems (UAV or UAS) have become a popular means of remotely gathering information and assessing infrastructure conditions due to their versatile nature. Multirotor and fixed-wing are two types of UAVs that are frequently used in field operations. The main application was to apply the technology for conducting military-related operations including the collection of reconnaissance videos before the war. Since then, UAVs have been used in other applications including averting potential risks to human life by eliminating the need for a pilot to carry out inspections tasks in hazardous conditions (*59*). After the introduction of Part 107 exemption of UAV operations by FAA in August 2016, more studies have been planned and performed with UAVs, evaluating their abilities to perform infrastructure condition assessments.

Advancements in compact mobile sensors complementing the development of unmanned aerial platforms have led to a remote and safe collection of the infrastructure condition data (*60*). Aerial platforms offer quick and high-quality information regarding the condition of the infrastructure asset. They also offer the two most desired characteristics for data collection. Accessibility to hard-to-reach areas and mobility in covering relatively large areas put these aerial platforms ahead of the traditional data collection methods. They also help in collecting a vast amount of infrastructure data that includes images in different views, elevations, overlaps, and resolutions. The data obtained from these aerial platforms serve as a digital history of the infrastructure behavior that helps to estimate the durability and plan timely rehabilitation strategies.

3.3.2. Civil Engineering Applications of UAVs

Rathinam et al. (*61*) conducted fixed wing UAV-based monitoring of linear structures such as roads, pipelines, bridges, and canals. Linear structures were detected by visual recognition techniques controlled by a closed-loop algorithm.

Bermis et al. (*62*) captured structural geology using ground-based and aerial-based photogrammetry datasets. They highlighted that lighting conditions, duration of the survey, and image network geometry influenced the quality of photogrammetric models. They conducted

semi-automatic identification of the faults of a rock slope in an orthorectified image and found to match the geometry and lengths of faults identified manually on a digitized map.

Many previous studies used UAVs to monitor landslides. Most of these studies had captured the condition of the landslide prone area and compared it with the pre-event digital data available either from satellites or other traditional methods (*63-66*). Previous studies also classified rock mass from aerial images captured using UAVs (*67, 68*).

Some studies conducted research on using multiple sensors to obtain and superimpose multiple bandwidths of object data for a better understanding of the infrastructure condition. Eschmann and Wundsam (*69*) used unmanned aerial platforms to carry a combination of customized sensors for the inspection of infrastructure assets. They used an optical camera, thermal imager, and Light Detection and Ranging (LiDAR) to obtain different attributes of the infrastructure condition. LiDAR data was used to obtain accurate point cloud data overlain by the texture obtained from the RGB camera. Thermal imaging was helpful in identifying the presence of moisture. A multitude of sensors on the remotely operating aerial platforms provides in-depth assessment of asset conditions. However, the increase in payload capacity significantly decreases the flight time and, thereby, reducing the coverage area per battery set.

Puppala et al. (*70*) used UAV platforms to identify pavement heaving caused by high sulfate soils. They were able to obtain the longitudinal elevation profiles along the wheel paths to spot any unusual elevation differences along the pavement surface. Congress et al. (*71*) conducted a comprehensive calibration analysis of drones and camera accessories to understand their compatibility for obtaining accurate data.

Recent studies have revealed an active engagement of several DOTs in research and implementation of UAV-assisted infrastructure asset management (*5, 72*). Caltrans Division of Engineering's geotechnical services has been involved in research projects using UAVs to perform geotechnical investigations about landslides, slope movements, and other steep terrain analyses (*73*).

3.3.3. Stability Analysis using Aerial Data

Several previous studies have utilized remotely collected aerial data to complement the slope stability analyses with geographical information (*7, 45, 74-77*). Saroglou et al. (*75*) used a UAV mounted with a camera to map a rock slope near the island of Lefkada, Greece that was subjected to earthquake forces. They attempted to identify the rockfall trajectory from the impact points identified in the 3D mapping products generated from the aerial images. They could not map the original trajectory due to the limitations of the available 2D analysis software. However, they were able to predict the actual trajectory by performing a 3D analysis. Nagendran et al. (*45*) and Congress et al. (*7*) conducted stability analyses on two different rock slopes, located in the northern region of Peninsular Malaysia and Texas, USA, respectively. They developed 3D models of the sloping topography from 2D photographs using the structure from motion (SFM) photogrammetric technique.

Nagendran et al. (*45*) used the LEM-based 2D and 3D analyses software to obtain the FOS of the slope. The 2D analysis was conducted on a section extracted from a 3D global minimum slope surface. Nagendran et al. (*45*) found that the FOS from the 3D deterministic analysis was higher compared to 2D deterministic analysis. Additionally, they also discussed the reasons behind

different FOS values. Firstly, the 2D analysis adopted over-conservative simplification, whereas actual 3D geometry was considered in the 3D analysis. Secondly, the 3D analysis considered both strong and weak rock surfaces to identify the failure surface. Congress et al. (*7*) conducted a 3D limit equilibrium slope stability analysis of a rock-cut and compared the critical FOS values obtained from Bishop's, Janbu's, and Morgenstern-Price's methods. They considered generalized Hoek-Brown failure criterion for rock-cut material. Congress et al. (*7*) observed that the FOS obtained from Morgenstern-Price's method was higher than the other two methods, which is consistent with the findings of previous studies about the relatively conservative nature of Bishop's and Janbu's methods.

4. METHODOLOGY

4.1. Laboratory Testing Plan

Five buckets of disturbed soil samples were collected from an embankment site with slope failure at the intersection of I-10 and Bluebonnet Blvd. in Baton Rouge, LA. A series of geotechnical tests were performed on the collected soils, which includes Atterberg limits tests (liquid limit, LL, and plastic limit, PL) (*78*), standard Proctor compaction test (*79*), sieve and hydrometer analyses (*80, 81*), and soil-water retention (SWR) or soil-water characteristics curve (SWCC) tests. The liquid and plastic limit tests determine the soil consistency and are used to classify the soil samples using the unified soil classification and system (USCS). In addition, the maximum dry unit weight (γ_{max}) and the optimum moisture content (ω_{opt}) for the soil samples were obtained from the compaction tests, by means of the moisture and dry unit curve. Pressure plate test and filter paper test were used to obtain the soil-water characteristic curve (SWCC). Then the measured SWCC curve was fitted with van Genuchten (*82*) and Fredlund and Xing (*83*) models. Figure 1 shows the ground view of the failed embankment.

Figure 1. Failed embankment site at I-10 and Bluebonnet Blvd., Baton Rouge, LA.

The LL and PL tests were performed on five samples from each bucket and observed results were 51 and 21, respectively. The plasticity index of the soil was 30. As per USCS, the soil was classified as high plasticity clay (CH). Figure 2 shows some of the performed tests.

Table 1. Atterberg Limits and Soil Classification

Description	Final Results
Liquid Limit, LL (%)	51
Plastic Limit, PL (%)	21
Plasticity Index, PI (%)	30
USCS Classification	**CH**

(a) (b) (c)

Figure 2. Soil testing (a) Sieve analysis, (b) liquid limit, and (c) compaction tests.

4.1.1. Standard Proctor Test

Standard Proctor compaction tests were performed, and the compaction curve was plotted in Figure 3. The soil was tested at five different moisture contents resulting in a maximum dry unit weight of 98.4 lb/ft^3 and an optimum moisture content of 21.5%. The resulting $\gamma_{d,\,max}$ and ω_{opt} are reported in Table 2.

Table 2. Maximum Dry Density and Optimum Moisture Content

Soil Sample	$\gamma_{d,\,max}$ (lb/ft^3)	ω_{opt} (%)
I-10/BB site	98.4	21.5

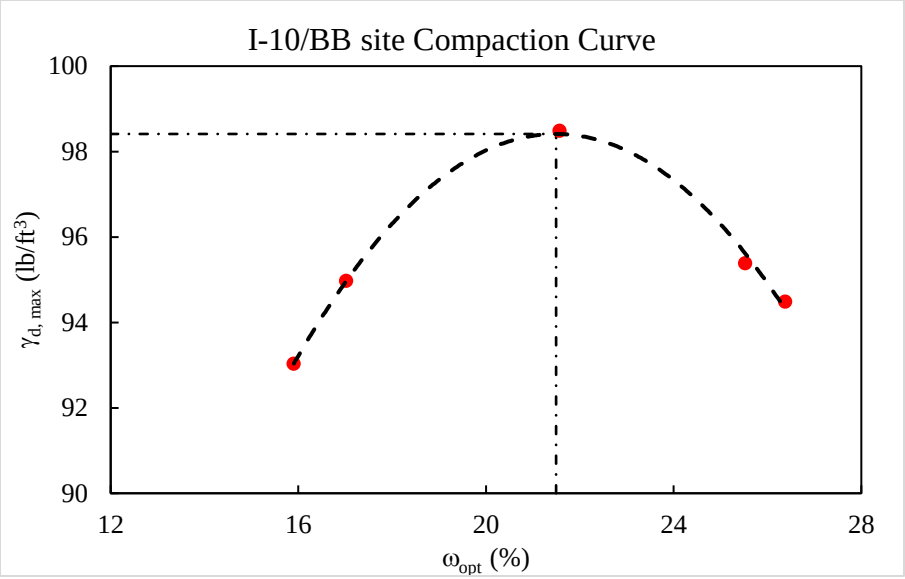

Figure 3. Standard Proctor compaction curve for the I-10/Bluebonnet Blvd intersection site.

Stark and Hussain (*84*) and Gamez and Stark (*85*) developed shear strength correlations with liquid limit (LL) and clay fraction size (CF). These correlations provide residual and fully softened strengths. At various effective normal stresses, residual and fully softened shear strengths were obtained from the measured liquid limit and clay fraction values of 51 and 33, respectively. The fully softened secant friction angles are provided at normal effective stresses of 12, 50, 100, and 400 kPa, and the resulting strength envelopes. Different equations are used to determine the friction angle according to the values of CF and LL, as shown in Figure 4. For the 12 kPa effective normal stress trendline, equation 1 is used when CF $\leq$ 20% and 30% $\leq$ LL $\leq$ 80%. Likewise, equation 2 is used when 25% $\leq$ CF $\leq$ 45% and 30% $\leq$ LL $\leq$ 130%. Finally, equation 3 is used when CF $\geq$ 50% and 30% $\leq$ LL $\leq$ 300%. Similar equations are available for higher effective normal stresses (*84*, *85*).

$$\phi'(\mathrm{LL}) = 35.33 - 5.85 \times 10^{-2}(\mathrm{LL}) + 9.71 \times 10^{-5}(\mathrm{LL})^2 \quad (1)$$

$$\phi'(\mathrm{LL}) = 38.10 - 1.19 \times 10^{-1}(\mathrm{LL}) + 2.48 \times 10^{-4}(\mathrm{LL})^2 \quad (2)$$

$$\phi'(\mathrm{LL}) = 36.45 - 9.18 \times 10^{-2}(\mathrm{LL}) - 1.09 \times 10^{-4}(\mathrm{LL})^2 + 1.10 \times 10^{-7}(\mathrm{LL})^3 \quad (3)$$

Figure 4. Fully softened secant friction angles for 12-kPa effective normal stress equations (*85*).

The above-mentioned strength parameters were incorporated in the strength stability analysis presented herein.

Figure 5 presents the residual and fully softened strength envelope for various effective normal stresses obtained from the measured liquid limit and clay fraction size values.

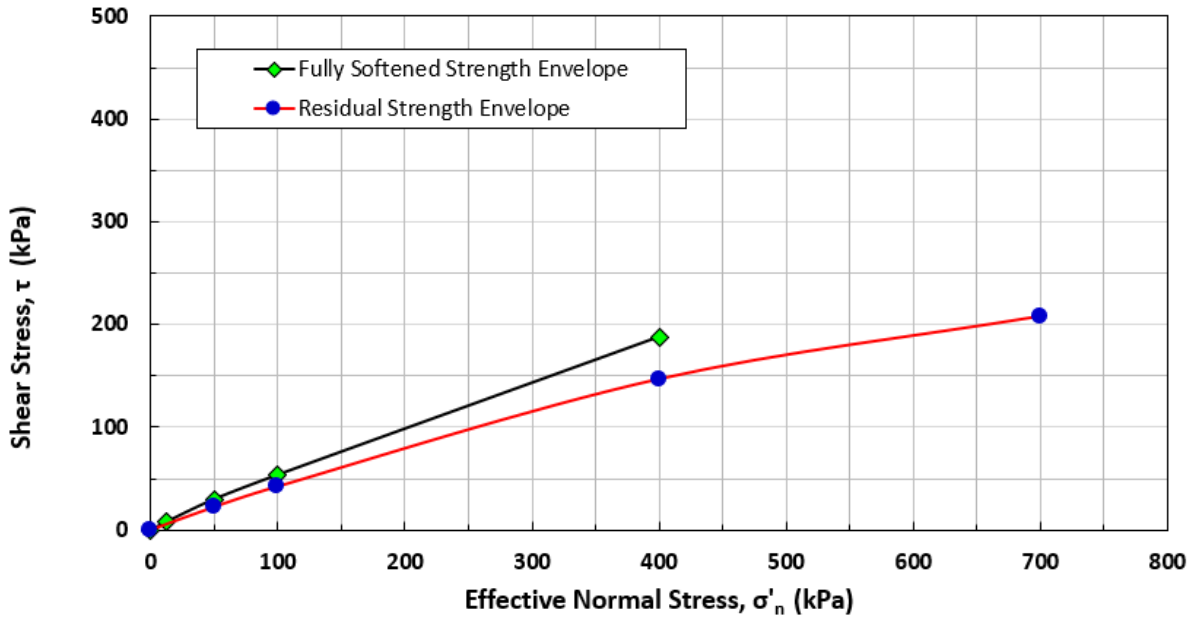

Figure 5. Fully softened and residual strength envelopes developed from Stark and Hussain (*84*) and Gamez and Stark (*85*) correlations

Additional to the field samples obtained for the tests mentioned in this section, the authors also planned to sample undisturbed blocks to perform torsional ring shear tests and compare the results with those of triaxial compression tests. Measuring field and laboratory soil-water retention curves was also planned for this project. Nevertheless, because a failure had occurred in the study site, the construction to repair the embankment started before going to the field and obtaining an undisturbed block sample was possible. Alternatively, the authors conducted preliminary tests with similar soils from a nearby embankment with similar characteristics as the soil's site. The results matched with published correlations and thus, the correlations were used to determine the strength envelopes. Soil-water retention curves in the field were not obtained because the embankment was an active construction site.

4.1.2. SWCC Test

Soil specimens for the SWCC test were compacted at 95% of $\gamma_{d,max}$ and ω_{opt} obtained from the standard Proctor test results. Soil matric suction was measured using the pressure plate method (*86*) for low suction and filter paper method (*87*) for high suction. Cylinder disk soil specimens of 2.254 in. diameter and 0.914 in. height were prepared using static compression with two lifts. Figure 6 shows six compacted soil specimens and the pressure plate test apparatus. Figure 7 shows the compacted soil specimens for the filter paper test. Figure 8 shows the sealed jar with soil specimens inside for moisture equilibrium.

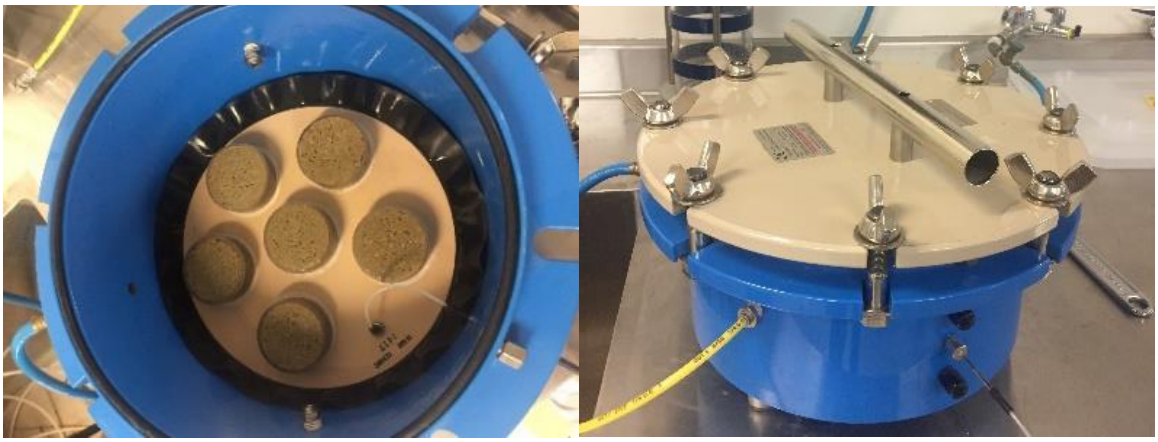

Figure 6. Six specimens inside the pressure plate chamber (left); pressure plate apparatus with locked cover (right)

Figure 7. Two stacked soil specimens with a filter paper in-between (left); filter paper sealed with electrical tape

Figure 8. Soil specimens inside a sealed jar for moisture equilibration

The measured oven-dry gravimetric water content was converted to volumetric water content and was compared to the applied air pressure (matric suction) for the pressure plate method. On the other hand, the matric suction (in log kPa) for the filter paper method was determined from the moisture content of the middle filter paper by using the calibration of Bulut et al. (*88*). The relationship resulting from the two methods was further examined by constructing a best fitting curve by the use of the van Genuchten (*82*) model, as shown in Figure 9. The SWCC of bucket 2 and bucket 3 were combined, and models of van Genuchten (*82*) and Fredlund (*83*) were constructed to find the best fitting curve (Figure 9); the two curves were consistent. Finally, the residual and saturated volumetric moisture content (θ_r and θ_s) were estimated, and the van

Genuchten empirical parameters (α, n, and m) were calculated. Similarly, the air-entry matric suction, ψ_r, and θ_s, as well as the Fredlund and Xing empirical parameters (a, n, and m), were calculated. These values are reported in Table 3.

Table 3. Soil-water retention properties using the van Genuchten (1980) model

van Genuchten (1980)	**θ_r (cm^3/cm^3)**	**θ_s (cm^3/cm^3)**	**α (-)**	**n (-)**	**m (-)**
	0.05	0.492	0.00007	0.397	3.942
Fredlund and Xing (1994)	**ψ_r (kPa)**	**a (-)**	**n (-)**	**m (-)**	**θ_s (m^3/m^3)**
	150000	1083.538	0.471	1.701	0.492

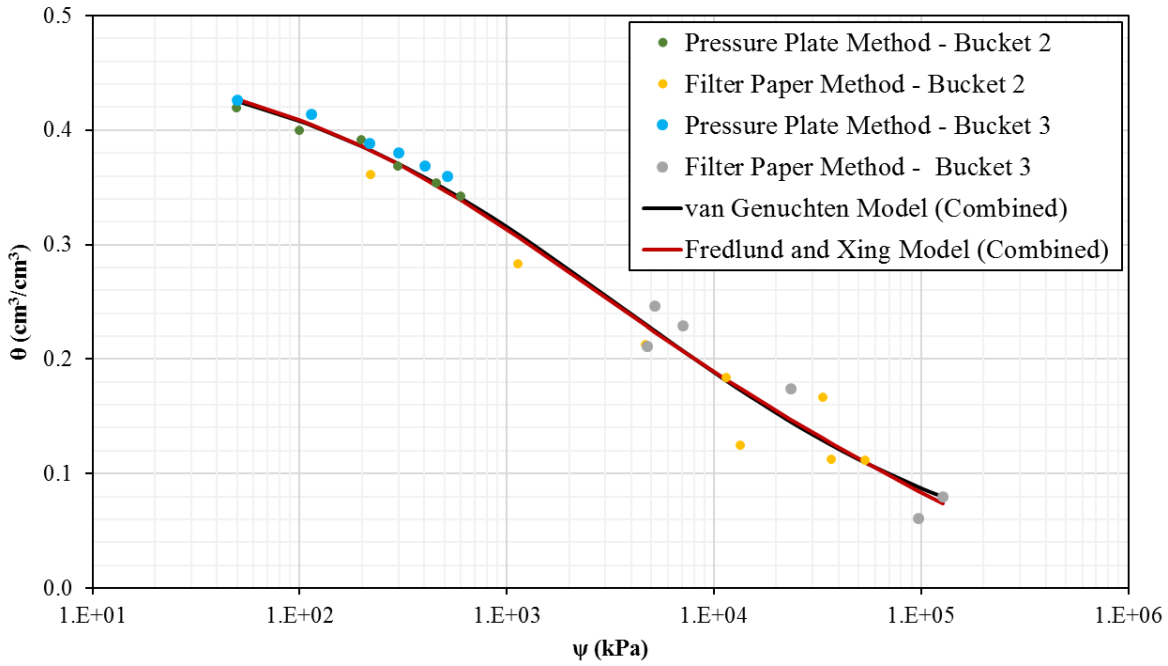

Figure 9. Measured SWCC curves and fitted models

4.2. Development and Testing of a suction-TDR sensor

This section presents detailed information, including materials and the calibration method for developing a suction-TDR probe. Currently, measurements of SWCC curves in the field mainly depend on two sensors, tensiometers for measuring soil matric suction and moisture meters for soil water content. Although commercial products can measure suction or moisture content with high accuracy, the correlation between the obtained soil matric suction and water content is questionable, stemming from the separate installation of moisture and suction sensors. Accordingly, a new moisture/suction TDR probe has been developed (*26*), as shown in Figure 10.

Two stainless steel rods were fabricated, as shown in Figure 10, to function as a transmission line probe. The steel rods were bent in the middle to divide the probe into two portions. The first portion has 0.2-inch spacing (5 mm), and the second portion has 1 inch (25 mm) spacing. This two-portion design allows for distinctive impedance difference between them and, therefore, easy detection of the material interface from TDR waveforms at the middle of the probe. The first portion is

embedded in a gypsum block, which is used for measuring matric suction. The suction-TDR sensor is embedded in soil to measure soil suction and moisture content. The gypsum block equilibrates with the testing soil, and the probe signal, i.e., a waveform, is acquired to determine the dielectric constant of the gypsum and the testing soil simultaneously. A dielectric constant and matric suction relationship for the gypsum can be established through a laboratory calibration procedure. As the gypsum has the same matric suction as the testing soil at equilibrium, the soil suction can be determined from the dielectric constant of the gypsum block using the calibration equation. The probe suction calibration can be accomplished through pressure plate tests and filter paper tests to establish a relationship between matric suction (ψ) and dielectric constant (K_a) for the gypsum block. Total three probes of three different probe diameters, 0.063 inches (1.6 mm), 0.079 inches (2 mm), and 0.118 inches (3 mm), were fabricated to study the effect of probe diameter and find the optimized sensor diameter.

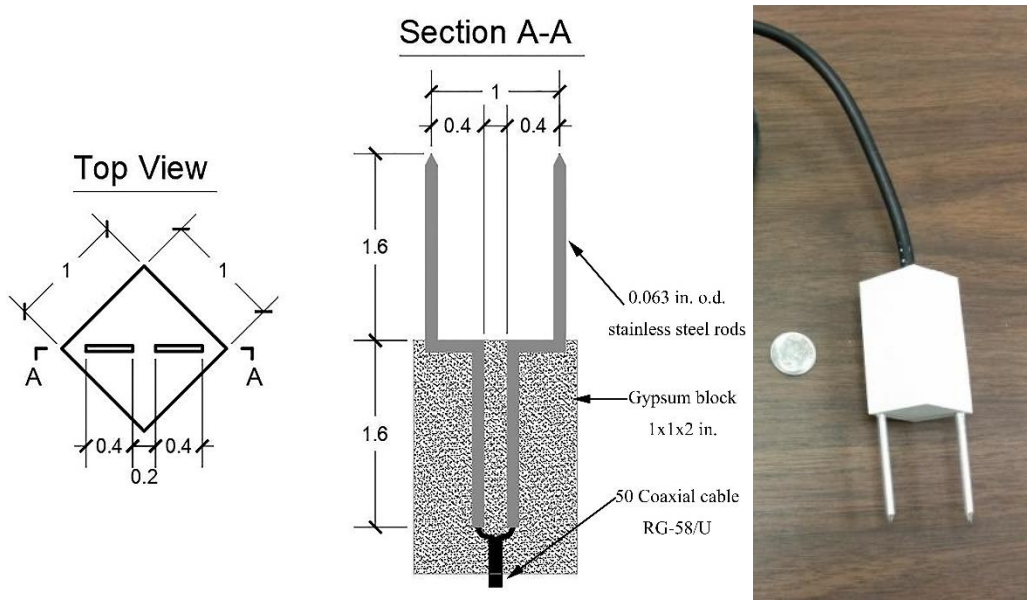

(a) (b)

Figure 10. Design of a moisture/suction TDR probe: (a) drawings, (b) photo of the probe (after Zhang et al. 2017)

The suction probes were calibrated for suction measurements using a pressure plate test, as shown in Figure 11. A suction probe was first saturated with distilled water and then was placed on the ceramic plate (15 bar) and sealed with a cover for testing. Different air pressures (7.5, 4.0, 2.0, 1.0, 0.8, 0.5, 0.3, 0.1 bar) were applied to the pressure plate chamber. After equilibrium at each pressure, the sensor was taken out for the acquisition of a TDR waveform. Then the waveform was analyzed to determine the dielectric constant of the gypsum block. Figure 12 shows the calibrations for the three probes. Because the dielectric constant of a gypsum block is correlated to its moisture content, an equation similar to the van Genuchten (*82*) equation was used to fit the experimental data to establish the calibration relationship between Ka and ψ as shown in Figure 12. Through waveform analyses and model fitting, the probe with a 2 mm diameter provides the best performance. Therefore, this probe was used for further laboratory evaluation.

Figure 11. A suction-TDR inside a pressure plate chamber for calibration of suction measurement

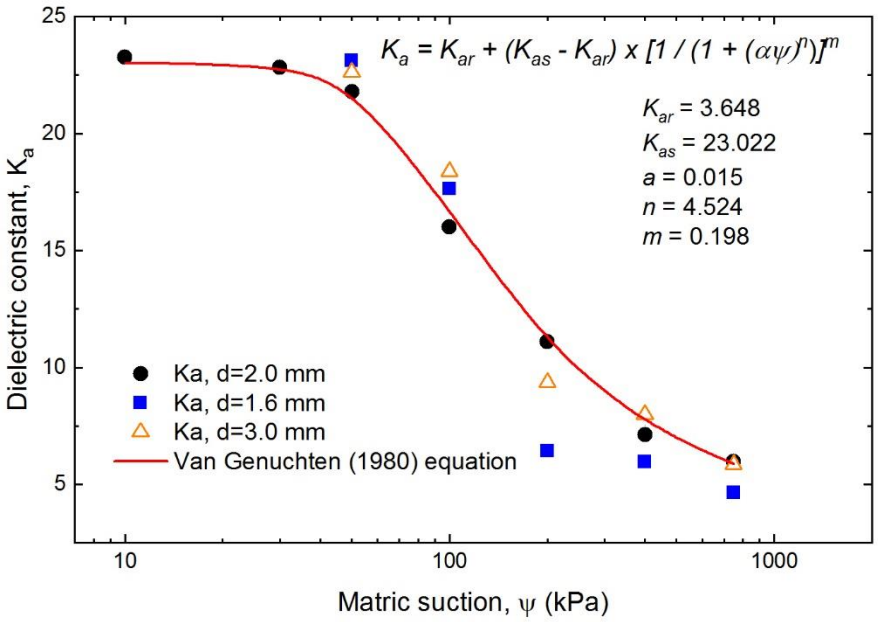

Figure 12. Matric suction vs. dielectric constant of the gypsum block for three probes

The suction-TDR sensor's performance was evaluated in silty sand (SM) soil. The test soil was classified as silty sand (SM) according to the Unified Soil Classification System (USCS). The specific gravity test was conducted to obtain the specific gravity of the soil solids. Atterberg limit tests conducted passing the #4 fraction classified the soil as non-plastic. It is reported that the maximum dry density of the silty sand is 1.87 g/cm^3, and the corresponding optimum moisture content is 12 %. All the soil properties are listed in Table 4.

Table 4. Soil properties and grain sizes of the silty sand used for evaluation of the suction-TDR sensor (*89*)

Sand (%)	55
Silt (%)	37
Clay (%)	8
Specific gravity, G_s	2.67
USCS classification	Silty sand (SM)
Maximum dry unit weight, ρ_{dmax} (g/cm^3)	1.87
Optimum moisture content, w (%)	12

Three different tests, staged-drying test, absorption, and desorption test, were conducted to evaluate the performance of the suction-TDR probe. The test setup is shown in Figure 13. The staged-drying test aims to measure the soil suction at different moisture contents and compare the results with the suction measurements by the Tempe cell method in the study by Patil (2014) (*89*). The silty sand sample was first compacted at the optimum moisture content 12% to achieve a target dry density of 1.87 g/cm^3. The compacted sample has the same moisture and dry density as in Patil (2014) (*89*) and is assumed to have the same SWCC curve as Patil (2014) (*89*). The suction-TDR was embedded inside the soil at the middle height of the soil column. Then the sample was dried by a mechanical fan until 9% moisture content was reached. The moisture content was measured by measuring the moisture loss of the sample on a high accuracy balance. The soil was continued to be dried to the moisture content of 6% and 3% following the same procedure. After enough equilibrium time at 3% moisture content, the same amount of water loss during the entire stage-drying process was poured onto the top surface of the sample to start the absorption test. After equilibrium at the end of the absorption test, the soil with a moisture content of 12% was dried with a mechanical fan for the desorption test. The desorption test was stopped when the moisture content reached 3%. The absorption and desorption test can study the equilibrium time of the gypsum block in the silty sand for suction measurement.

The comparison of measured suction by the suction-TDR probe with those obtained by the Tempe cell test in Patil (2014) (*89*) study is shown in Figure 14. It is obvious that the suction measurement from the two different methods agreed with each other very well in the moisture content range 3%<w<12%. However, the performance of the new probe in the moisture content range, i.e., w>12.2% or w<3%, was not examined in the staged drying test. The change of suction over time during the desorption test is shown in Figure 15. The suction measured from the suction-TDR sensor was obtained from the measured dielectric constant of the gypsum using the calibration equation shown in Figure 12. The suction measurement was also estimated from the gravimetric water content using the SWCC curve obtained in Patil (2014) (*89*). Comparing with the results from the Tempe cell experiments in Patil (2014) (*89*) study, it is found that the measured suction by the probe is always lower than the Tempe cell experiments at suction levels below 300 kPa, and it reaches the actual value after 10-20 h. This is because the moisture flow driven by the matric suction from the gypsum block to the specimen takes time to get the suction equilibrium between them. However, a good agreement was observed at a higher suction range from 300 kPa to 2000 kPa. This is because the higher suction accelerated the speed of moisture flow from the gypsum block to the specimen and reduced the time needed to attain the suction equilibrium. In addition,

the measured suction at 250 h was much lower than that obtained from the Tempe cell experiment since the calibration relationship for suction measurement was limited within a suction range between 10 and 750 kPa. Thus, the probe may not be applicable to soils at a higher suction range.

Figure 13. Test setup for evaluation of the suction-TDR sensor performance in silty sand

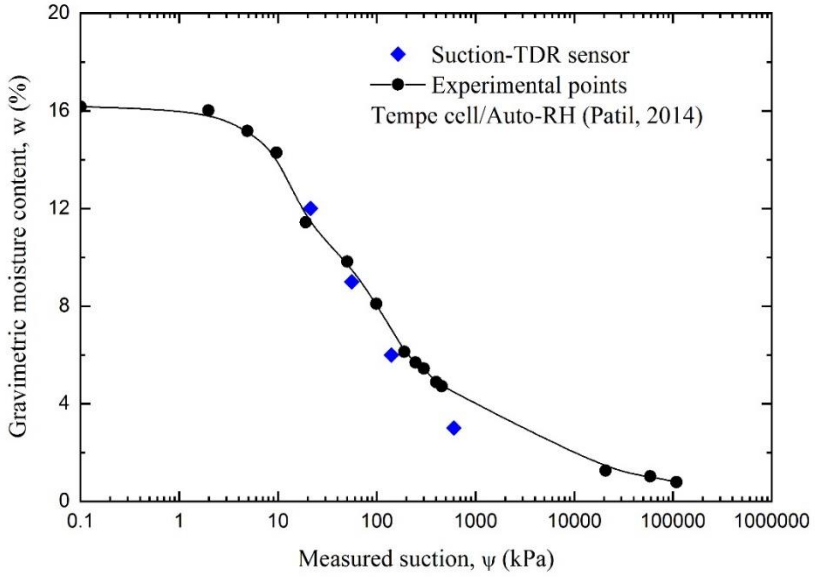

Figure 14. Comparison of suction-TDR sensor measurement in silty sand against the SWCC obtained by Tempe cell

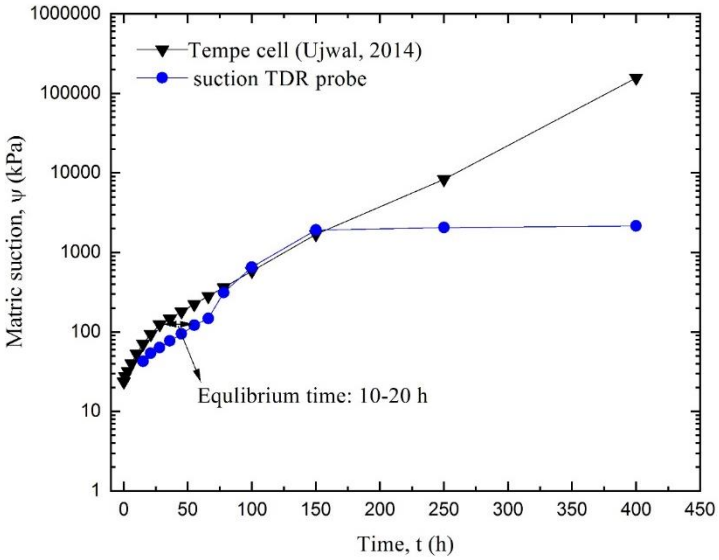

Figure 15. Comparison of suction-TDR sensor measurement in silty sand against the SWCC obtained by Tempe cell during desorption test

4.3. Aerial Data Collection

Modern-day three-dimensional data analysis and visualization make it feasible for engineers and decision-makers to view the details of sites and perceive the condition of infrastructure assets in an intuitive way (*60*). Unmanned aerial vehicles, owing to their ability to view from different locations, is one of the most used platforms to collect three-dimensional data.

UAV data collection crew comprised of federal aviation administration (FAA) certified remote pilots in command (RPIC) and multiple visual observers (VO). The UAV data collection tasks are classified as preflight, mission flight, and postflight tasks executed using rotary UAV shown in Figure 16. Below are the steps carried out during the aerial data collection. Preflight tasks include the identification of airspace over the site location coordinates. FAA waiver was not required as the site is located within Class-G airspace. Weather details such as wind speed, humidity, and precipitation were verified to plan the flight tasks. Reconnaissance of the site was conducted using images collected by the research team and from google street view maps. The flight plan was prepared and modified based on the inputs from the reconnaissance survey.

Figure 16. Drone taking off for aerial inspection.

Flight missions comprised of different flights at different altitudes and viewpoints. First, the whole area was captured by flying at an average altitude of 20 m and camera in nadir direction with an 80% overlap. Later, the camera was inclined and flown at an average altitude of 13 m to capture detailed information about the failure. In total, 240 images were collected during all flights spanning under 18 minutes in total. Flights had to be delayed due to the unexpected inclement weather. Post-flight operations included data retrieval procedures and debriefing of the data collection tasks. The geotagged images were retrieved, and a quick quality check of the collected imagery was performed by building a low-quality model at the field before packing all the equipment. This was to ensure that there were no holes formed due to a lack of enough overlap between images (*71*). The low-quality model can be observed in Figure 17. For quantitative inspections, the geotagged image data was used to process the image alignment, point cloud generation, rendering of mesh & texture, and ortho-rectification. A fully navigable digital elevation model (DEM), in addition to a dense point cloud, mesh, and orthomosaics are some of the 3D mapping products obtained to analyze the failed embankment slope.

(a)

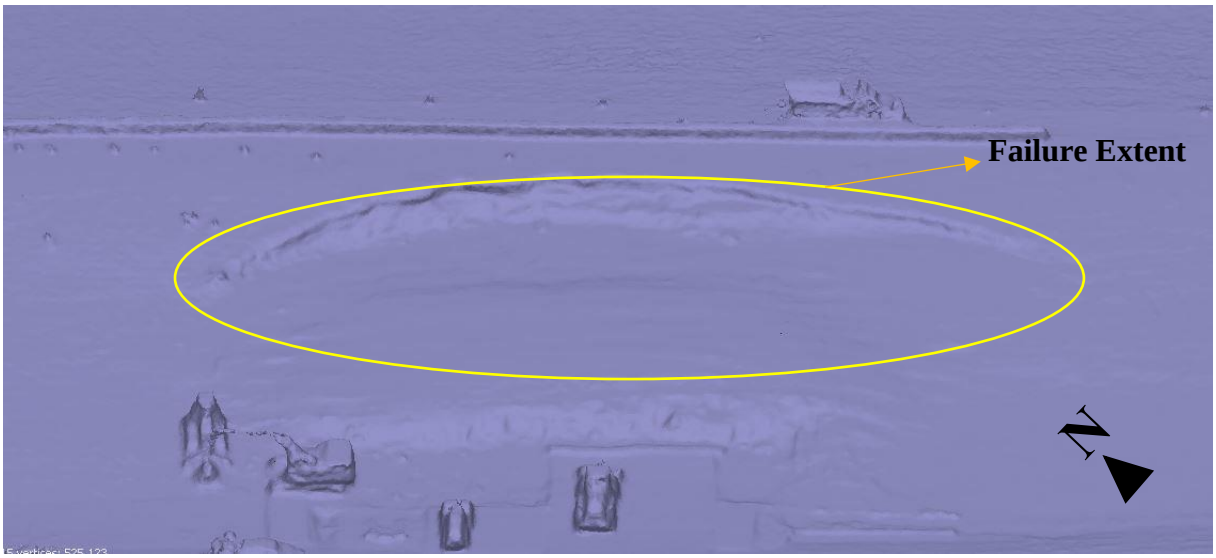

(b)

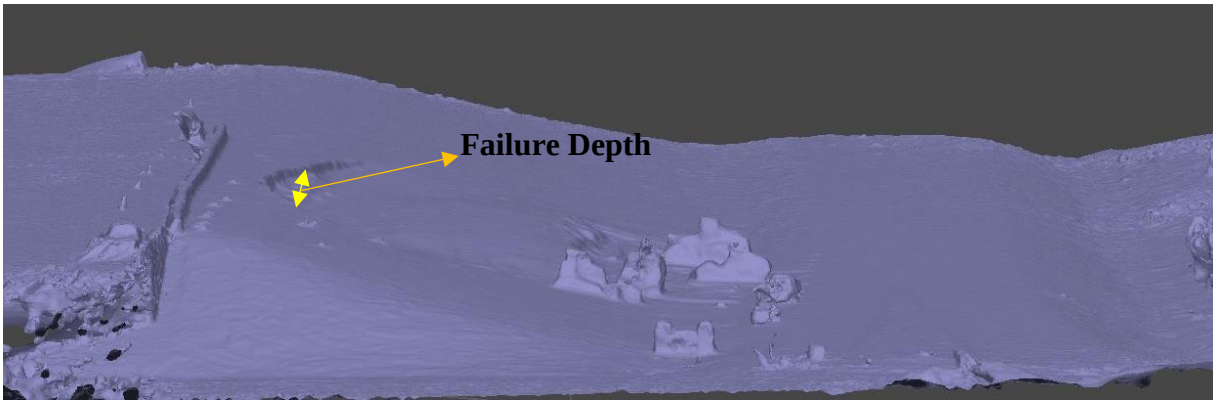

(c)

Figure 17. Three-dimensional Mapping products of the failed embankment section (a) Orthomosaic (b) Front view of the Elevation Model (c) Side view of the Elevation Model.

The photogrammetric model was able to provide the relative extent of the failed section of the embankment as shown in Figure 17b. The ability to view the model in multiple formats with each pixel depicting either the RGB values or height information is valuable towards understanding the slope failure mechanism.

5. ANALYSIS AND FINDINGS

5.1. Back analysis using UAV data

When compared to the orthomosaic shown in Figure 17, the dense point cloud obtained from UAV-CRP technology (Figure 18a) can be observed to depict the exact conditions existing in the field during the time of the unmanned aerial inspection. Each point in the model was associated with X, Y, and Z location information that provides the surficial geometry of the embankment slope safely and efficiently. Besides, the equipment being used to repair the failure can also be observed in Figure 18, more prominently in the solid model generated using the depth maps derived from the 2D aerial images.

(a)

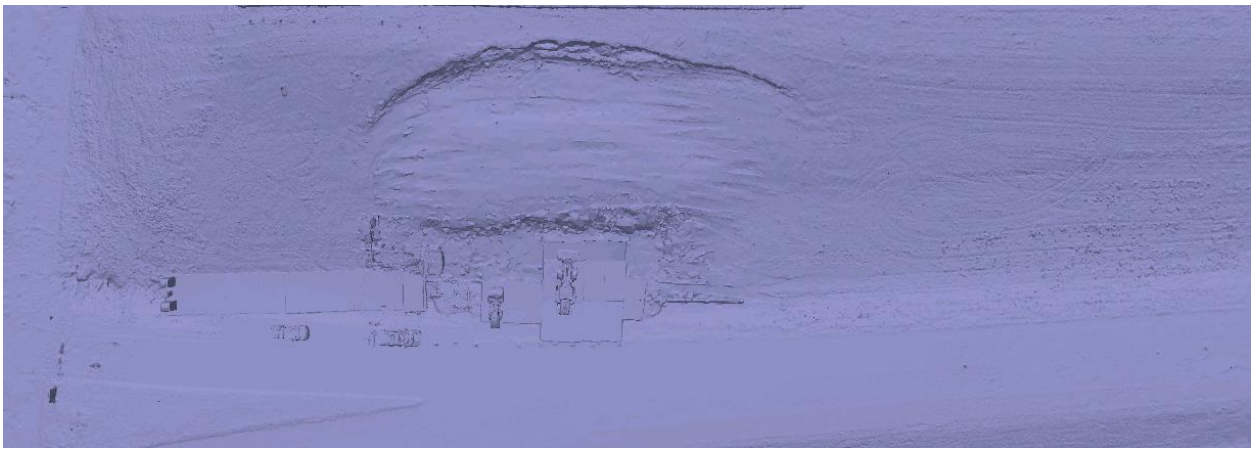

(b)

Figure 18. Failed embankment (a) dense point cloud (b) solid model

5.2. Two-dimensional (2D) Back Analysis

The two-dimensional (2D) back analysis was conducted on a section obtained from the 3D model developed using the aerial images (Fig. 19). The 2D intact slope surface and the failure surface were obtained from the 3D model. The clayey soil embankment slope was segregated into two regions: compacted core soil and topsoil within 2.0 m from the slope surface. The current 2D analysis considered both seepage and stability analyses of the slope. The 2D seepage analysis was conducted using a commercially available finite element method (FEM) based software (*90*). This analysis considered both saturated and unsaturated water flows, and the van Genuchten (*82*) model was used for the coefficient of permeability of unsaturated soil. As recommended by Qi and Vanapalli (*91*), the coefficient of permeability of topsoil was increased by 500 times that of the core soil to consider the effect of desiccation cracks. The coefficient of permeability for core soil and topsoil were considered to be 1.0×10^{-7} and 5.0×10^{-5}, respectively. The groundwater table was defined at 2.0 m below the ground surface. An influx boundary was considered to simulate rainfall conditions at the soil-atmospheric interface. Due to persistent rainfall that happened before the slope failure, rainfall intensity of 20 mm/h and duration of rainfall up to 5 days were considered for the analysis. At the base, on both sides above the groundwater table, a no-flow boundary condition was considered. The 2D stability analysis was conducted using a commercially available limit equilibrium method (LEM) based software to determine the factor of safety of slope (*92*).

The pore water pressures from seepage analysis were used for the calculation of FOS at each time step in the stability analysis. The Mohr-Coulomb failure criterion was used for both core soil and topsoil. Additionally, the Vanapalli et al. (*93*) model was used to model the shear strength of unsaturated soils. Spencer's method, which satisfies both force and moment equilibriums, was used to determine the FOS. The fully softened shear strength properties (cohesion = 0 kPa & friction angle = 25°), obtained from the above correlations, were used for the topsoil layer. For core soil, the shear strength properties (cohesion = 8 kPa & friction angle = 23°) obtained from the direct shear test were used. The soil-water characteristic curve (SWCC) was obtained from the software's database using saturated volumetric water content and soil type.

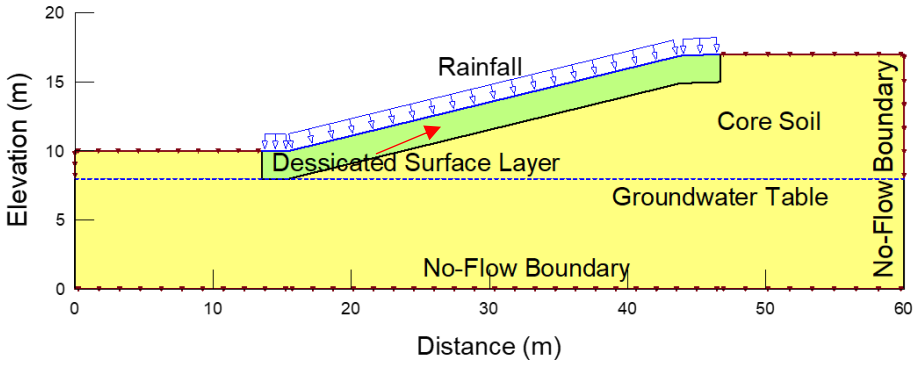

(a)

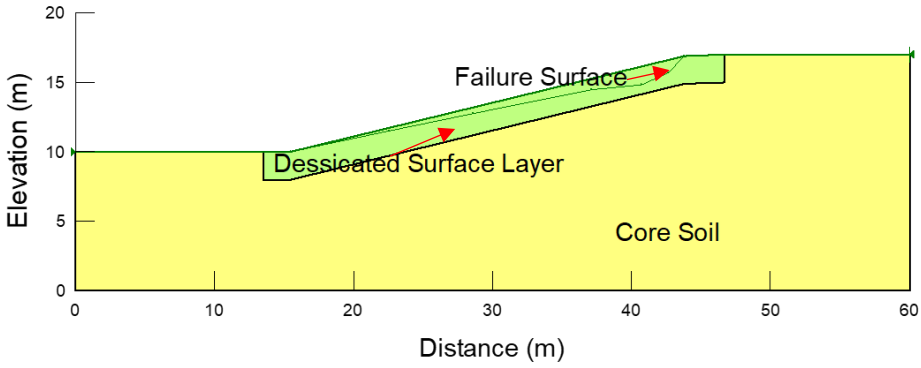

(b)

Figure 19. 2D analysis of embankment slope geometry (a) Seepage analysis (b) Slope Stability analysis

The FOS of the slope was obtained as 0.91 after 1 day of rainfall duration and observed to be approximately constant up to 5 days of rainfall. Hence, these failure conditions for 1 day of rainfall duration were used further to back-calculate the material characteristics at FOS of 1.0. The cohesion and friction angle were obtained as 0 kPa and 27°, respectively.

5.3. Three-dimensional (3D) Back Analysis

The dense point cloud obtained from UAV-CRP technology (Fig. 20) can be observed to depict the exact conditions existing in the field during the time of the unmanned aerial inspection. Each point in the model was associated with X, Y, and Z location information that provides the surficial geometry of the embankment slope safely and efficiently. Besides, the equipment being used to repair the failure can also be observed in Fig. 20, more prominently in the solid model generated using the depth maps derived from the 2D aerial images.

One of the advantages of the 3D mapped products obtained from the UAV-CRP technology is the ability to use the digital replica for various purposes. In this case, the dense point cloud was used to not only remove the unwanted points representing the construction equipment but also to re-create the approximate embankment slope surface before failure. The dense point cloud model was cleaned and edited to obtain two surfaces, i.e., after and before failure, of the embankment shown in Figs 20a and 20b, respectively. Fig. 20a shows the surface of the failed embankment without the construction equipment. The elevations of the points surrounding the failed area were used to interpolate a surface before failure. Extruding the 2D slope section adopted during the time of construction and recreating the embankment is one of the alternatives to using this approximate surface before failure. However, lack of access to some of these records and the change in the geometry of embankment during its service period are a few challenges identified for this alternative. Hence, the approximate intact embankment slope generated from UAV-CRP technology was used in conjunction with the failed surface to conduct back analysis. 1-m elevation contours also provide a better idea about the surface profile existing before and after failure.

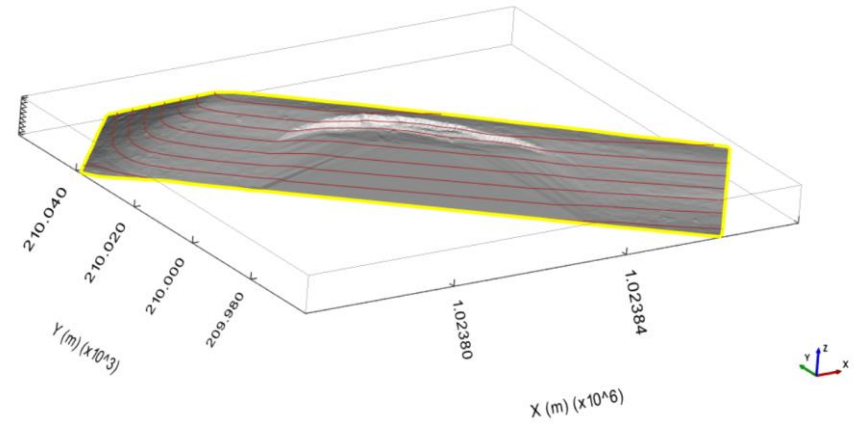

(a)

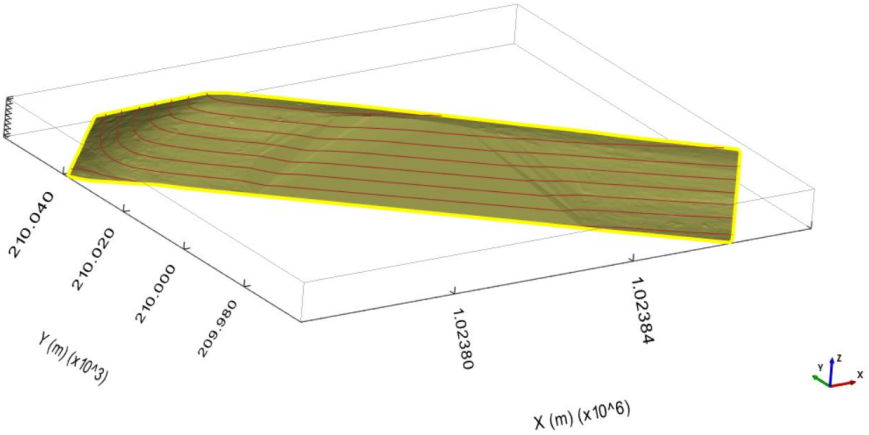

(b)

Figure 20. Embankment conditions with 1-m contours (a) after failure (b) before failure

The failure of the embankment depends upon various factors such as the loading, climatic conditions, type of soil, the geometry of soil, and others. A commercial 3D slope stability software was used to input the 3D models of the intact slope as the top surface and the failed slopes as the basal surface to back-calculate the soil parameters at failure (*94*). The cross-section view of the 3D model depicting intact embankment slope with the failure surface underneath can be observed in Fig. 21. This slope was analyzed based on the Mohr-Coulomb failure criterion using Spencer's method. Based on the type of soil and the laboratory testing, an approximate range of the effective angle of internal friction and cohesion was provided as 0-30° and 0-10 kPa, respectively. Persistent rainfall events were observed to be the cause of failure so the embankment at the time of failure was assumed to have extreme conditions with a water table close to the ground surface. This provides the material characteristics for the worst possible scenario, which can be used to design resilient embankment slopes to withstand extreme weather events in the future. The number of iterations for each parameter was set to 40 and generated 1600 points, shown in Fig. 22. The contours of the factor of safety values corresponding to those points were calculated and provided

in Fig. 22. It can be observed that the soil characteristics at the time of failure may have existed along the factor of safety value of 1.0. Considering the negligible cohesion exhibited by these soils, the range of friction angle values obtained from the 3D back analysis is close to the values obtained from the laboratory tests and the 2D back analysis of failed slope. The lack of consideration of end effects in the 2D slope stability analysis may have contributed to its higher friction angle values compared to the back calculated values from the 3D analysis.

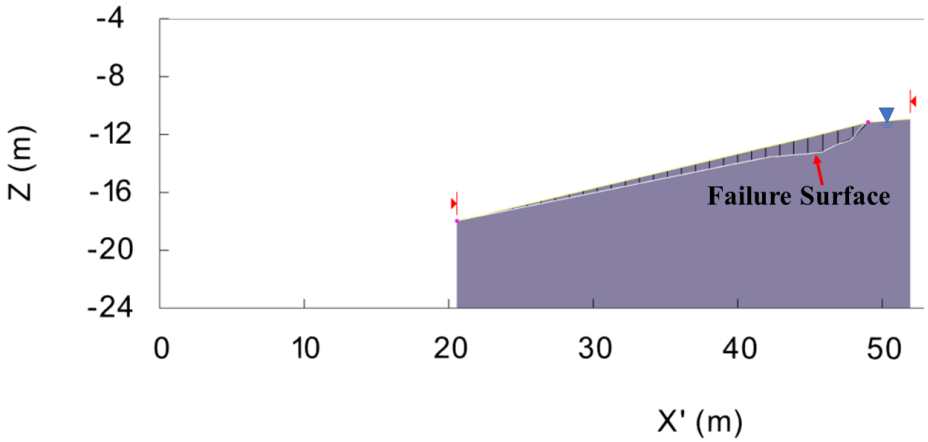

Figure 21. Cross-sectional view of the intact and the failed embankment slope models used in 3D back analysis

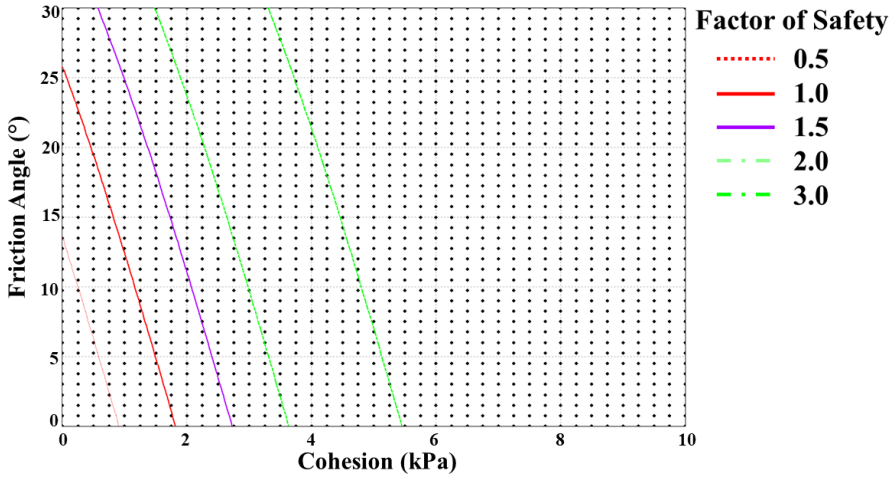

Figure 22. 3D back analysis results depicting various combinations of material characteristics for each factor of safety

6. CONCLUSIONS

The soil collected from the failed embankment site was tested for soil classification, compaction, and SWCC curve. The collected soils have both CH and CL clays. The SWCC test results show a repeatable SWCC curve among the tested soils and high suction at low moisture content. A new suction-TDR probe was developed based on the TDR technique to measure the soil moisture content and matric suction simultaneously. The calibration equation for suction measurement was obtained by pressure plate test, while the calibration relationship for soil moisture content measurement was established by a staged-drying test. The evaluation of the probe was performed through three tests on silty sand: staged-drying test, absorption test, and desorption test. The test results revealed that: (1) the suction-TDR probe could measure moisture content rapidly and accurately in wetting and drying processes; (2) the response time of the dry gypsum block in moist specimen with a moisture content of 12% is around 48 h; (3) the probe can measure the suction satisfactorily in drying process at a suction range between 300 kPa and 2000 kPa, whereas the equilibrium time of the gypsum block is around 10-20h at suction levels below 300 kPa; (4) the probe is only applicable in the suction range from 10 to 2000 kPa, and it may underestimate soil suction at higher suction levels. The applicability of the probe in other soil types still needs to be studied in the future. In addition, the calibration curve for suction measurement can be extended by other methods (e.g., filter paper method) for soils at the higher suction range

Comprehensive laboratory testing helps in designing the stability of embankment slopes conservatively. However, the stability of the slope depends upon various conditions existing in the field. The increase in the frequency of the natural disasters contributed by climate change has posed unique challenges to geotechnical engineers. Some of these include subjecting the geotechnical infrastructure to extreme conditions. Alternate wetting and drying cycles create weak planes within the soil mass to allow the seepage of rain water and accelerate the slope failure before the intended design period. Hence, there is a need to do a forensic analysis of the failed assets for a better understanding of the failed conditions and incorporating those findings in future designs.

This study used unmanned aerial vehicle-based close-range photogrammetry technology to map the existing failed slope section and back-calculate the soil conditions at failure. The back-calculated soil characteristics were observed to be within the range of the soil parameters calculated from the laboratory testing of the soil samples collected at the failed site. It also provides an idea about other existing conditions that may have prompted the failure, which in this case is the rise in the water table due to rain events. Comprehensively documenting the failed embankment slopes will also provide inputs to ensure the sustainability and resiliency of transportation infrastructure assets.

All the lessons learned from this investigation will be included in the upcoming report “Static and Seismic Slope Stability, Volume 1: Drained Soil Shear Strengths” prepared by Dr. Timothy Stark at the University of Illinois at Urbana-Champaign (*95*).

REFERENCES

1. Skempton, A. Slope stability of cuttings in brown London clay.In *Selected Papers on Soil Mechanics*, Thomas Telford Publishing, 1984. pp. 241-250.

2. Wright, S. G. Evaluation of soil shear strengths for slope and retaining wall stability analyses with emphasis on high plasticity clays. 2005.

3. Puppala, A. J., T. Manosuthikij, and B. C. S. Chittoori. Swell and shrinkage characterizations of unsaturated expansive clays from Texas. *Engineering Geology*, Vol. 164, 2013, pp. 187-194.

4. George, A. M., S. Chakraborty, J. T. Das, A. Pedarla, and A. J. Puppala. Understanding Shallow Slope Failures on Expansive Soil Embankments in North Texas Using Unsaturated Soil Property Framework.In *PanAm Unsaturated Soils 2017*, 2018. pp. 206-216.

5. Puppala, A. J., and S. S. C. Congress. A Holistic Approach for Visualization of Transportation Infrastructure Assets Using UAV-CRP Technology. *International Conference on Inforatmion Technology in Geo-Engineering*, 2019, pp. 3-17.

6. Siebert, S., and J. Teizer. Mobile 3D mapping for surveying earthwork projects using an Unmanned Aerial Vehicle (UAV) system. *Automation in Construction*, Vol. 41, 2014, pp. 1-14.

7. Congress, S. S. C., P. Kumar, U. D. Patil, T. V. Bheemasetti, and A. J. Puppala. Three-Dimensional Stability Analysis of Rock Slope Using Aerial Photogrammetry Data.In, American Society of Civil Engineers, Reston, 2020. pp. 388-398.

8. Congress, S. S. C., A. J. Puppala, N. H. Jafari, A. Banerjee, and U. D. Patil. The Use of Unmanned Aerial Photogrammetry for Monitoring Low-Volume Roads after Hurricane Harvey.In, TRB, Washington, D.C., Kalispell, 2019. pp. 15-15.

9. Jafari, N., S. S. C. Congress, A. J. Puppala, and H. M. Nazari. RAPID Collaborative: Data Driven Post-Disaster Waste and Debris Volume Predictions using Smartphone Photogrammetry App and Unmanned Aerial Vehicles. 2019.

10. Congress, S. S. C., and A. J. Puppala. Geotechnical slope stability and rockfall debris related safety assessments of rock cuts adjacent to a rail track using aerial photogrammetry data analysis. *Transportation Geotechnics*, Vol. 30, 2021, p. 100595.

11. Congress, S. S. C., A. J. Puppala, P. Kumar, A. Banerjee, and U. Patil. Methodology for Resloping of Rock Slope Using 3D Models from UAV-CRP Technology. *Journal of Geotechnical and Geoenvironmental Engineering*, Vol. 147, No. 9, 2021, p. 05021005.

12. Puppala, A. J., S. S. C. Congress, T. V. Bheemasetti, and S. Caballero. Geotechnical Data Visualization and Modeling of Civil Infrastructure Projects.In, Springer, 2018. pp. 1-12.

13. Rathje, E. M., K.-s. Woo, and M. Crawford. Spaceborne and airborne remote sensing for geotechnical applications.In, 2006. pp. 1-19.

14. Shamsabadi, S. S., M. Wang, and R. Birken. PAVEMON: a GIS-based data management system for pavement monitoring based on large amounts of near-surface geophysical sensor data.In, 2014.

15. Suncar, O. E., E. M. Rathje, and S. M. Buckley. Deformations of a rapidly moving landslide from high-resolution optical satellite imagery.In, 2013. pp. 269-278.

16. Tahar, K. N., and A. Ahmad. A simulation study on the capabilities of rotor wing unmanned aerial vehicle in aerial terrain mapping. *International Journal of Physical Sciences,* Vol. 7, No. 8, 2012, pp. 1300-1306.

17. Robinson, D. A., C. S. Campbell, J. W. Hopmans, B. K. Hornbuckle, S. B. Jones, R. Knight, F. Ogden, J. Selker, and O. Wendroth. Soil moisture measurement for ecological and hydrological watershed-scale observatories: A review. *Vadose Zone Journal,* Vol. 7, No. 1, 2008, pp. 358-389.

18. Drnevich, V. P., X. Yu, and J. E. Lovell. Beta testing implementation of the Purdue Time Domain Reflectometry (TDR) method for soil water content and density measurement. 2003.

19. Yu, X., and V. P. Drnevich. Soil water content and dry density by time domain reflectometry. *Journal of Geotechnical and Geoenvironmental Engineering,* Vol. 130, No. 9, 2004, pp. 922-934.

20. White, N. K. Accuracy and bias of TDR measurements in compacted sands. 2004.

21. Pan, H., Y. Qing, and L. Pei-yong. Direct and Indirect Measurement of Soil Suction in the Laboratory. *Electronic Journal of Geotechnical Engineering,* Vol. 15, 2010, pp. 1-14.

22. Klute, A., G. S. Campbell, and G. W. Gee. Water Potential: Miscellaneous Methods.In *Methods of Soil Analysis: Part 1—Physical and Mineralogical Methods,* Soil Science Society of America, American Society of Agronomy, Madison, WI, 1986. pp. 619-633.

23. Klute, A., D. K. Cassel, and A. Klute. Water Potential: Tensiometry.In *Methods of Soil Analysis: Part 1—Physical and Mineralogical Methods,* Soil Science Society of America, American Society of Agronomy, Madison, WI, 1986. pp. 563-596.

24. Noborio, K., R. Horton, and C. S. Tan. Time domain reflectometry probe for simultaneous measurement of soil matric potential and water content. *Soil Science Society of America Journal,* Vol. 63, No. 6, 1999, pp. 1500-1505.

25. Zhang, N., X. B. Yu, and A. Puppala. Design and Evaluation of a Moisture/Suction TDR Probe. *Geotechnical Testing Journal,* Vol. 40, No. 5, 2017, pp. 762-775.

26. Zhang, N., X. B. Yu, and A. Pradhan. Application of a thermo-time domain reflectometry probe in sand-kaolin clay mixtures. *Engineering Geology,* Vol. 216, 2017, pp. 98-107.

27. Yu, X., N. Zhang, and P. Asheesh. Development and Evaluation of a Thermo-TDR Probe.In *GeoShanghai 2014: Soil Behavior and Geomechanics,* Shanghai, 2014. pp. 434-444.

28. Yu, X., P. Asheesh, N. Zhang, S. Tjuatja, and B. Thapa. Thermo-TDR Probe for Measurement of Soil Moisture, Density, and Thermal Properties.In *Geo-Congress 2014 Technical Papers*, 2014. pp. 2804-2813.

29. Baumgartner, N., G. W. Parkin, and D. E. Elrick. Soil-Water Content and Potential Measured by Hollow Time-Domain Reflectometry Probe. *Soil Science Society of America Journal*, Vol. 58, No. 2, 1994, pp. 315-318.

30. Whalley, W. R., P. B. Leedsharrison, P. Joy, and P. Hoefsloot. Time-Domain Reflectometry and Tensiometry Combined in an Integrated Soil-Water Monitoring-System. *Journal of Agricultural Engineering Research*, Vol. 59, No. 2, 1994, pp. 141-144.

31. Durner, W., and D. Or. Soil Water Potential Measurement.In *Encyclopedia of Hydrological Sciences*, John Wiley & Sons, Ltd, 2006.

32. Lungal, M., and B. C. Si. Coiled time domain reflectometry matric potential sensor. *Soil Science Society of America Journal*, Vol. 72, No. 5, 2008, pp. 1422-1424.

33. Toker, N. K., J. T. Germaine, K. J. Sjoblom, and P. J. Culligan. A new technique for rapid measurement of continuous soil moisture characteristic curves.In *Géotechnique, No. 54*, 2004. pp. 179-186.

34. Whalley, W. R., C. W. Watts, M. A. Hilhorst, N. R. A. Bird, J. Balendonck, and D. J. Longstaff. The design of porous material sensors to measure the matric potential of water in soil. *European Journal of Soil Science*, Vol. 52, No. 3, 2001, pp. 511-519.

35. Jones, S. B., J. M. Wraith, and D. Or. Time domain reflectometry measurement principles and applications. *Hydrological Processes*, Vol. 16, No. 1, 2002, pp. 141-153.

36. Lam, L., and D. G. Fredlund. A general limit equilibrium model for three-dimensional slope stability analysis. *Canadian Geotechnical Journal*, Vol. 30, 1993, pp. 905-919.

37. Xing, Z. Three-Dimensional Stability Analysis of Concave Slopes in Plan View. *Journal of Geotechnical Engineering Engineering*, Vol. 114, No. 8, 1988, pp. 658-671.

38. Leshchinsky, D., and C.-c. Huang. Generalized three-dimensional slope-stability analysis. *Journal of Geotechnical Engineering*, Vol. 118, No. 11, 1992, pp. 1748-1764.

39. Michalowski, R. L. Limit analysis and stability charts for 3D slope failures. *Journal of Geotechnical and Geoenvironmental Engineering*, Vol. 136, No. 4, 2010, pp. 583-593.

40. Pham, H. T. V., and D. G. Fredlund. The application of dynamic programming to slope stability analysis. *Canadian Geotechnical Journal*, Vol. 40, No. 4, 2003, pp. 830-847.

41. Lorig, L., and P. Varona. *Numerical analysis. Rock Slope Engineering. Civil and Mining*. Spon Press, London and New York, 2007.

42. Leong, E. C., and H. Rahardjo. Two and three-dimensional slope stability reanalyses of Bukit Batok slope. *Computers and Geotechnics,* Vol. 42, 2012, pp. 81-88.

43. Nian, T. K., R. Q. Huang, S. S. Wan, and G. Q. Chen. Three-dimensional strength-reduction finite element analysis of slopes: Geometric effects. *Canadian Geotechnical Journal,* Vol. 49, 2012, pp. 574-588.

44. Bolla, A., and P. Paronuzzi. Geomechanical Field Survey to Identify an Unstable Rock Slope: The Passo della Morte Case History (NE Italy). *Rock Mechanics and Rock Engineering*, No. 0123456789, 2019.

45. Nagendran, S. K., M. A. Mohamdad Ismail, and Y. T. Wen. 2D and 3D rock slope stability assessment using Limit Equilibrium Method incorporating photogrammetry technique. *Bulletin of the Geological Society of Malaysia,* Vol. 68, No. December 2019, 2019, pp. 133-139.

46. Gitirana, G., M. A. Santos, and M. D. Fredlund. Three-dimensional analysis of the Lodalen landslide. *Geotechnical Special Publication*, No. 178, 2008, pp. 186-190.

47. Wines, D. A comparison of slope stability analyses in two and three dimensions. *Journal of the Southern African Institute of Mining and Metallurgy,* Vol. 116, No. 5, 2016, pp. 399-406.

48. Bolla, A., and P. Paronuzzi. Numerical Investigation of the Pre-collapse Behavior and Internal damage of an unstable rock slope. *Rock Mechanics and Rock Engineering*, 2019.

49. Pourkhosravani, A., and B. Kalantari. A Review of Current Methods for Slope Stability Evaluation. *Electronic Journal of Geotechnical Engineering,* Vol. 16, 2011.

50. Egeli, I., and H. F. Pulat. Mechanism and modelling of shallow soil slope stability during high intensity and short duration rainfall. *Scientia Iranica,* Vol. 18, No. 6, 2011, pp. 1179-1187.

51. Khan, S. A., and S. M. Abbas. Numerical modelling of highway embankment by different ground improvement techniques. *International Journal of Innovative Research in Advance Engineering*, Vol. 1, No. 10, 2014, pp. 350-356.

52. Rouainia, M., T. O'Brien, O. Davies, and S. Glendinning. Numerical modelling of climate effects on slope stability. *Proceedings of the ICE - Engineering Sustainability,* Vol. 162, No. 2, 2009, pp. 81-89.

53. Cerato, A., R. Oleski, and C. Puklin. *Case Study: Compacted Embankment Landslide in Grady County, Oklahoma*. 2006.

54. Khan, M. S., S. Hossain, A. Ahmed, and M. Faysal. Investigation of a shallow slope failure on expansive clay in Texas. *Engineering Geology,* Vol. 219, 2017, pp. 118-129.

55. Cerato, A. B., Y. Hong, X. Yu, X. He, and W. Tabet. Real time monitoring of slope stability in eastern Oklahoma.In, Oklahoma. Dept. of Transportation. Planning and Research Division, 2014.

56. Titi, H. H., and S. Helwany. Investigation of Vertical Members to Resist Surficial Slope Instabilities. 2007.

57. Wu, T. H., C. M. Kokesh, B. R. Trenner, and P. J. Fox. Use of Live Poles for Stabilization of a Shallow Slope Failure. *Journal of Geotechnical and Geoenvironmental Engineering*, Vol. 140, No. 10, 2014, p. 05014001.

58. Congress, S. S. C. Novel Infrastructure Monitoring Using Multifaceted Unmanned Aerial Vehicle Systems - Close Range Photogrammetry (UAV - CRP) Data Analysis.In, 2018.

59. Haulman, D. L. US unmanned aerial vehicles in combat, 1991-2003.In, AIR FORCE HISTORICAL RESEARCH AGENCY MAXWELL AFB AL, 2003.

60. Puppala, A. J., S. S. C. Congress, T. V. Bheemasetti, and S. R. Caballero. Visualization of Civil Infrastructure Emphasizing Geomaterial Characterization and Performance. *Journal of Materials in Civil Engineering*, Vol. 30, No. 10, 2018, pp. 04018236-04018236.

61. Rathinam, S., Z. W. Kim, and R. Sengupta. Vision-based monitoring of locally linear structures using an unmanned aerial vehicle. *Journal of Infrastructure Systems*, Vol. 14, No. 1, 2008, pp. 52-63.

62. Bemis, S. P., S. Micklethwaite, D. Turner, M. R. James, S. Akciz, S. T. Thiele, and H. A. Bangash. Ground-based and UAV-Based photogrammetry: A multi-scale, high-resolution mapping tool for structural geology and paleoseismology. *Journal of Structural Geology*, Vol. 69, 2014, pp. 163-178.

63. Lucieer, A., S. M. d. Jong, and D. Turner. Mapping landslide displacements using Structure from Motion (SfM) and image correlation of multi-temporal UAV photography. *Progress in Physical Geography: Earth and Environment*, Vol. 38, No. 1, 2014, pp. 97-116.

64. Niethammer, U., M. R. James, S. Rothmund, J. Travelletti, and M. Joswig. UAV-based remote sensing of the Super-Sauze landslide: Evaluation and results. *Engineering Geology*, Vol. 128, 2012, pp. 2-11.

65. Stumpf, A., J.-P. Malet, N. Kerle, U. Niethammer, and S. Rothmund. Image-based mapping of surface fissures for the investigation of landslide dynamics. *Geomorphology*, Vol. 186, 2013, pp. 12-27.

66. Turner, D., A. Lucieer, and S. de Jong. Time Series Analysis of Landslide Dynamics Using an Unmanned Aerial Vehicle (UAV). *Remote Sensing*, Vol. 7, No. 2, 2015, pp. 1736-1757.

67. Salvini, R., C. Vanneschi, S. Riccucci, M. Francioni, and D. Gullì. Application of an integrated geotechnical and topographic monitoring system in the Lorano marble quarry (Apuan Alps, Italy). *Geomorphology*, Vol. 241, 2015, pp. 209-223.

68. Vollgger, S. A., and A. R. Cruden. Mapping folds and fractures in basement and cover rocks using UAV photogrammetry, Cape Liptrap and Cape Paterson, Victoria, Australia. *Journal of Structural Geology,* Vol. 85, 2016, pp. 168-187.

69. Eschmann, C., and T. Wundsam. Web-Based Georeferenced 3D Inspection and Monitoring of Bridges with Unmanned Aircraft Systems. *Journal of Surveying Engineering,* Vol. 143, No. 3, 2017, pp. 04017003-04017003.

70. Puppala, A. J., N. Talluri, S. S. C. Congress, and A. Gaily. Ettringite induced heaving in stabilized high sulfate soils. *Innovative Infrastructure Solutions,* Vol. 3, No. 1, 2018, pp. 72-72.

71. Congress, S. S. C., A. J. Puppala, and C. L. Lundberg. Total system error analysis of UAV-CRP technology for monitoring transportation infrastructure assets. *Engineering Geology,* Vol. 247, 2018, pp. 104-116.

72. Tony, D. 35 State DOTs are Deploying Drones to Save Lives, Time and Money Survey Results Featured in Special Report Video: Building Highways in the Sky: State DOTs Leading the Evolution of Drones.In, 2018.

73. Karpowicz, R. The Use of Unmanned Aerial Systems for Steep Terrain Investigations - PDF.In, 2014.

74. Al-Rawabdeh, A., F. He, A. Moussa, N. El-Sheimy, and A. Habib. Using an unmanned aerial vehicle-based digital imaging system to derive a 3D point cloud for landslide scarp recognition. *Remote Sensing,* Vol. 8, No. 2, 2016, pp. 95-95.

75. Saroglou, C., P. Asteriou, D. Zekkos, G. Tsiambaos, M. Clark, and J. Manousakis. UAV-based mapping, back analysis and trajectory modeling of a coseismic rockfall in Lefkada island, Greece. *Natural Hazards & Earth System Sciences,* Vol. 18, No. 1, 2018.

76. Wang, S., Z. Zhang, C. Wang, C. Zhu, and Y. Ren. Multistep rocky slope stability analysis based on unmanned aerial vehicle photogrammetry. *Environmental earth sciences,* Vol. 78, No. 8, 2019, pp. 260-260.

77. Xie, M., T. Esaki, G. Zhou, and Y. Mitani. Geographic information systems-based three-dimensional critical slope stability analysis and landslide hazard assessment. *Journal of Geotechnical and Geoenvironmental Engineering,* Vol. 129, No. 12, 2003, pp. 1109-1118.

78. ASTM. D4318-17e1. Standard test methods for liquid limit, plastic limit, and plasticity index of soils.In, American Society for Testing and Materials International, 2018.

79. ---. D698-12 (2021). Standard Test Methods for Laboratory Compaction Characteristics of Soil Using Standard Effort (12 400 Ft-lbf/ft3 (600 KN-m/m3)).In, American Society for Testing and Materials International, 2012.

80. ---. D422-63 (2007). Standard test method for particle-size analysis of soils.In, American Society for Testing and Materials International, 2007.

81. ---. D7928-21e1. Standard test method for particle-size distribution (gradation) of fine-grained soils using the sedimentation (hydrometer) analysis.In, American Society for Testing and Materials International, 2021.

82. Van Genuchten, M. T. A closed-form equation for predicting the hydraulic conductivity of unsaturated soils. *Soil Science Society of America Journal*, Vol. 44, No. 5, 1980, pp. 892-898.

83. Fredlund, D. G., and A. Xing. Equations for the soil-water characteristic curve. *Canadian Geotechnical Journal*, Vol. 31, No. 4, 1994, pp. 521-532.

84. Stark, T. D., and M. Hussain. Empirical correlations: drained shear strength for slope stability analyses. *Journal of Geotechnical and Geoenvironmental Engineering*, Vol. 139, No. 6, 2013, pp. 853-862.

85. Gamez, J. A., and T. D. Stark. Fully Softened Shear Strength at Low Stresses for Levee and Embankment Design. *Journal of Geotechnical and Geoenvironmental Engineering*, Vol. 140, No. 9, 2014, p. 06014010.

86. ASTM. D5298-16. Standard test method for measurement of soil potential (suction) using filter paper.In, American Society for Testing and Materials International, 2016.

87. ---. D6836-16. Standard test methods for determination of the soil water characteristic curve for desorption using a hanging column, pressure extractor, chilled mirror hygrometer, and/or centrifuge.In, American Society for Testing and Materials International, 2016.

88. Bulut, R., R. L. Lytton, and W. K. Wray. Soil suction measurements by filter paper.In *Expansive clay soils and vegetative influence on shallow foundations*, 2001. pp. 243-261.

89. Patil, U. D. *Response of unsaturated silty sand over a wider range of suction states using a novel double-walled triaxial testing system*. The University of Texas at Arlington, 2014.

90. GeoSlope. Seepage Modeling with SEEP/W.In, Calgary, Alta, 2020.

91. Qi, S., and S. K. Vanapalli. Stability analysis of an expansive clay slope: a case study of infiltration-induced shallow failure of an embankment in Regina, Canada. *International Journal of Georesources and Environment-IJGE (formerly Int'l J of Geohazards and Environment)*, Vol. 1, No. 1, 2015, pp. 1-1): 7-19.

92. GeoSlope. Stability Modeling with GeoStudio.In, Calgary, Alta, 2020.

93. Vanapalli, S., D. Fredlund, D. Pufahl, and A. Clifton. Model for the prediction of shear strength with respect to soil suction. *Canadian Geotechnical Journal*, Vol. 33, No. 3, 1996, pp. 379-392.

94. TAGASoft. TSLOPE Technical Information.In, 2022.

95. Stark, T. D., and A. Idries. *Static and Seismic Slope Stability, Volume 1: Drained Soil Shear Strengths*. First Draft Complete for Review by ASCE Publishing, 2021.